CMS Draft Analysis Note

2010/06/08
Head Id: 7720
Archive Id: 7724M
Archive Date: 2010/06/04
Archive Tag: trunk

Transverse Momentum Distribution within Jets in pp Collisions at $\sqrt{s}$=7 TeV

Anwar A Bhatti[1], Vivain, O'Dell[2], Kenichi Hatakeyama[3], Ozdemir Kadri[4], and Pelin Kurt[5]

[1] The Rockefeller University, New York, NY 10065, USA
[2] Fermi National Accelerator Laboratory, Batavia IL 60510, USA
[3] Baylor University, Waco, TX 76706, USA
[4] Cukurova University, Adana, Turkey
[5] Vanderbilt University, Nashville, TN 37235, USA

Abstract

Using pp collisions at center of mass energy of 7 TeV collected by CMS detector at Large Hadron Collider at CERN, we have measured the jet shapes, defined as the fractional transverse momentum distribution as a function of the distance from the jet axis. Since jet shapes are sensitive to parton showering processes they provide a good test of Monte Carlo event simulation programs. In this note we present a study of jet shapes reconstructed using calorimeter energies using CMS data with $\sim$ 10 nb^{-1} of integrated luminosity. We compare the results with predictions of the QCD inspired event generators PYTHIA and HERWIG++. For PYTHIA predictions, various underlying event tunes were studied.

Contents

1 Introduction

The transverse momentum profile of a jet, jet shapes [1, 2], is sensitive to multiple parton emissions from the primary outgoing parton and provides a good test of the parton showering description of Quantum Chromodynamics (QCD), the theory of strong interactions. Historically the jet shape has been used to test perturbative QCD (pQCD) α_s^3 calculations [3, 4]. These leading order calculations, with only one additional parton in a jet, showed good agreement with the observed jet shapes. While confirming the validity of pQCD calculations, jet shape studies also indicated that jet clustering, underlying event contribution and hadronization effects must be considered. Currently, these effects can be modeled accurately only within the framework of full-event generators. Current Monte Carlo (MC) event generators use pQCD inspired parton shower models, in conjunction with hadronization and underlying event models, to generate final state particles. MC generators are used extensively to model signal and background events in most analyses at hadron colliders. Jet shapes can be used to tune phenomenological parameters in these MC generators. QCD predicts broader gluon jets than quark jets. The structure of quark and gluon jets can be investigated by comparing measurements of the jet shapes in different processes enriched with either quark or gluon initiated jets in the final state. As

shown in Fig. 1, in QCD jet production, the gluon jet contribution changes with the transverse momenta of the jets. Previously, jet shapes have been measured in $p\bar{p}$ collisions at Tevatron and ep collisions at HERA [3–7]. In this paper, we present a study of jet shapes measured using calorimeter information in the central region of the CMS detector at $\sqrt{s} = 7$ TeV using integrated luminosity of xx nb^{-1}. and compare the results obtained with various MC generators. The sensitivities of jet shapes to the underlying event (UE) model and to the flavor of the initiating parton are also explored.

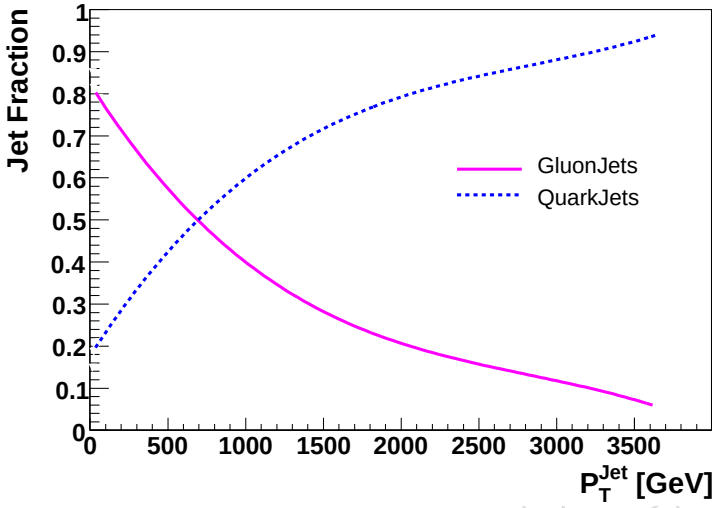

Figure 1: Fraction of the quark or gluon initiated jets as a function of jet p_T for $|y| < 1$ (from PYTHIA DWT) in pp scattering at $\sqrt{s} = 14$ TeV

2 Definition of Jet Shapes

The jet shape is defined as the average fraction of the jet transverse momentum within a cone of a given size r around the jet axis, $r = \sqrt{(y_i - y_j)^2 + (\phi_i - \phi_j)^2}$, where i refers to the particle, calorimeter tower or track, and j to the jet. Jet shapes can be studied by using an integrated or a differential distribution. In the present study only two leading jets within $|y| < 1$ are considered per event. All particles and calorimeter towers within distance $R = \sqrt{(\Delta y)^2 + (\Delta\phi)^2} = 0.7$ from the jet axis are used . This large cone size ensures that most of the parent parton energy is included in the jet. The differential distribution, $\rho(r)$, is illustrated in Fig. 5. It is defined as the fraction of the jet transverse momentum contained inside an annulus of inner radius $r - \delta r/2$ and outer radius $r + \delta r/2$ around the jet axis, such that $0 \leq r \leq R$:

$$\rho(r) = \frac{1}{\delta r}\frac{1}{N_{jet}}\sum_{jets}\frac{p_T(r - \delta r/2, r + \delta r/2)}{p_T(0, R)}. \quad (1)$$

Above, N_{jet} denotes the total number of selected jets. In the numerator p_T is the sum of all particles, tracks or towers in the distance range $(r - \delta r/2, r + \delta r/2)$ from the jet axis. In the denominator, $p_T(0, R)$ is the scalar sum of transverse momenta of all the particles, tracks or towers within the cone of radius R.

Similarly, the integrated jet shape (see Figure 6), $\psi(r)$, is defined as:

$$\psi(r) = \frac{1}{N_{jets}}\sum_{jets}\frac{p_T(0, r)}{p_T(0, R)} \quad (2)$$

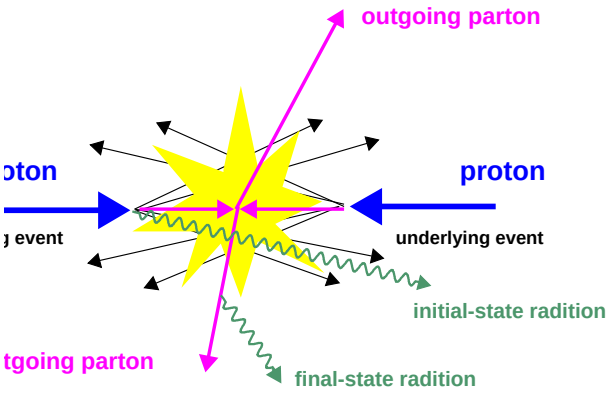

Figure 2: Illustration of a typical proton-proton two parton hard scattering event including initial and final state radiation and beam-beam remnants.

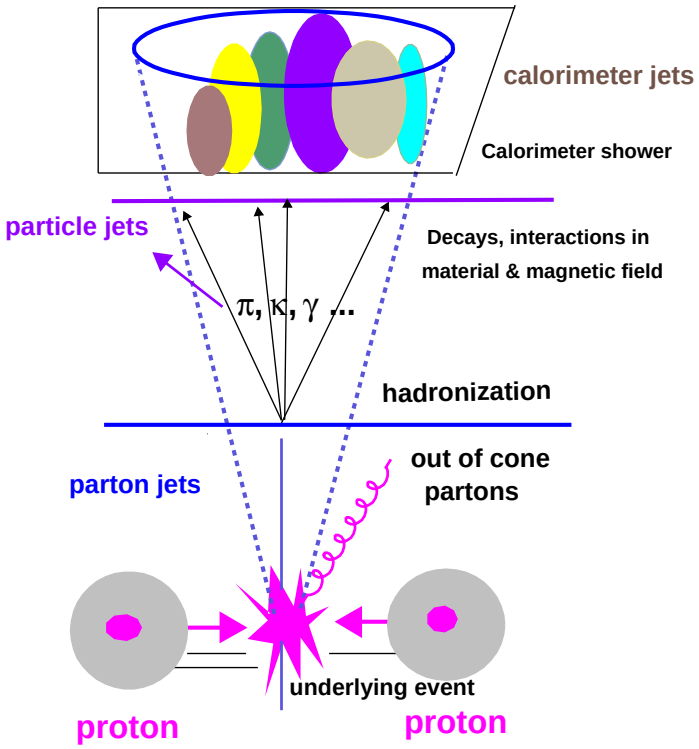

Figure 3: Schematic of jet evolution and detection. Parton jets hadronize into particle jets which interact in the calorimeter forming calorimeter jets.

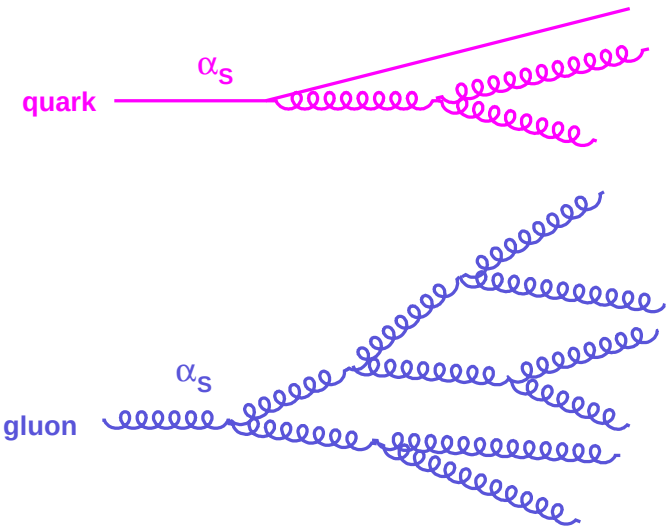

Figure 4: Examples of the structure of quark and gluon initiated jets

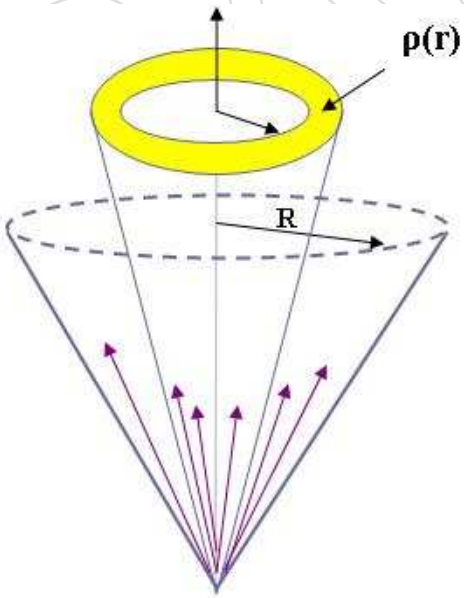

Figure 5: Definition of the differential jet shape, $\rho(r)$.

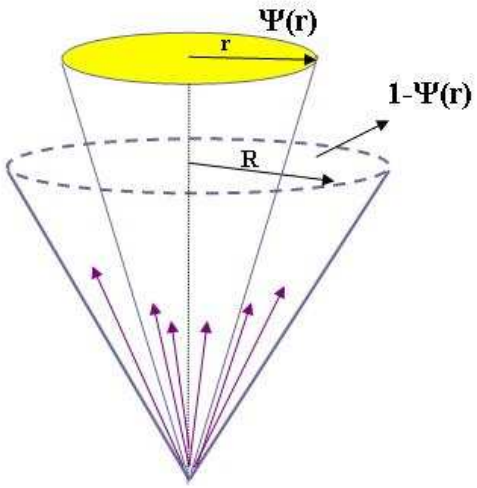

Figure 6: Definition of the integrated jet shape, $\psi(r)$.

where $p_{\mathrm{T}}(0, r)$ is the scalar sum of transverse momenta of all particles within the distance r from the jet axis with $\psi(r = R) \equiv 1$.

To calculate the jet shapes, we made histograms of transverse momentum in the appropriate bin of r divided by the transverse momentum in the cone $R = 0.7$. The mean value of these histograms was then plotted as function of r. The statistical uncertainty on each point was calculated as $rms/\sqrt{N}$, using the rms of the corresponding histogram and the number N of jets in the bin. For the integrated shape the uncertainties at different r points are partially correlated.

3 CMS Detector

The Compact Muon Solenoid (CMS) detector is a multipurpose apparatus at the Large Hadron Collider (LHC) at CERN. The CMS has a cylindrical structure covering almost 4π of angular phase-space in order to detect a large fraction of particles produced in a pp collision. It contains subsystems which are designed to measure energies and momenta of photons, electrons, muons, and hadrons [8–10].

The central hadronic section (HCAL) is made of brass and scintillators while the electromagnetic section (ECAL) comprises lead tungstate crystals ($PbWO_4$). The response of the calorimeter to photons is linear versus incident energy, while the response to hadrons depends strongly on the incident energy. The difference in response of the calorimeter to photons and hadrons leads to a nonlinear energy response of the calorimeter to jets.

The coordinate system used at CMS[11] is defined as follows: the x-axis points horizontally towards the LHC ring center, the y-axis points upwards, and the z-axis is aligned with the nominal anti-clock-wise beam direction. The azimuthal angle is ϕ and the polar angle is θ. The transverse momentum p_{T} is defined as a projection of a particle momentum P on the xy-plane, $p_{\mathrm{T}} = P \cdot \sin\theta$, and the "transverse energy" as $E_T = E \cdot \sin\theta$. The rapidity is defined as $y = \frac{1}{2} \log \frac{E+P_Z}{E-P_Z}$, where E denotes the energy and P_Z is the component of the momentum along the z direction. The pseudo-rapidity is defined as $\eta = -\ln[\tan\frac{\theta}{2}]$.

4 Jet Clustering Algorithms

In high energy interactions partons are produced in the final state with large transverse momenta as a result of the hard scattering process illustrated in Figure 2. Partons outgoing from the interaction point produce parton showers and subsequently partons from these showers combine to form hadrons which are color singlets which interact in the detector (see Figure 3). Since the transverse momenta involved in the hadronization process are much smaller than the hard scattering momenta, the final state particles are collimated around the direction of the original parton. These streams of particles are called jets. Jet clustering algorithms are used to associate particles to a particular jet. Direction and energy of a jet are related to the direction and energy of the original parton.

Many jet reconstruction algorithms are being used in CMS including iterative cone, k_{T}, SISCone (Seedless Infrared Safe Cone) [12] and anti-k_{T} algorithms [13]. The cone jet algorithm, such as SISCone, groups the input objects together based on their distance in (y, ϕ) space, and the determination of the jet quantities is done at the end of the jet finding. The successive recombination algorithms iteratively merge input objects into final jets and so the jet kinematic quantities, the jet direction and energy, are calculated directly during the clustering. In this analysis, the anti-k_{T} algorithm has been used to reconstruct jets with $D = 0.7$. The anti-k_{T} algorithm [13] starts with a list of proto-jets given by 4-momentum (E, p_x, p_y, p_z). All the objects which are to be clustered are considered as proto-jets. The transverse momentum p_{T}, rapidity y, and azimuthal angle ϕ of a proto-jet are calculated using give Equation 4.

$$(E, p_x, p_y, p_z) = \sum_i (E, p_x, p_y, p_z)_i \tag{3}$$

$$p_T = \sqrt{p_x^2 + p_y^2} \qquad y_c = \frac{1}{2} \ln \left(\frac{E + p_z}{E - p_z} \right) \qquad \phi_c = \tan^{-1}(p_y / p_x). \tag{4}$$

For each proto-jet i and the pair $(i, j,\ i \neq j)$, d_i and d_{ij} are defined as

$$d_i = p_{T,i}^2 \qquad d_{ij} = \min(p_{T,i}^{2p}, p_{T,j}^{2p}) \, \frac{(y_i - y_j)^2 + (\phi_i - \phi_j)^2}{D^2} \tag{5}$$

where D is the parameter which controls the size of the jet. For the anti-k_{T} algorithm, the parameter $p = -1$. The algorithm determines the minimum d_{min} of the d_i and all the d_{ij}. If $d_{min} = d_i$, the proto-jet is not mergable and is promoted to a jet. Otherwise, the proto-jets i, j are merged into a single proto-jet with the 4-momentum $(E_{ij}, \vec{p}_{ij}) = (E_i + E_j, \vec{p}_i + \vec{p}_j)$. The process is repeated until no proto-jets are left. In anti-k_{T} algorithm the measure d depends on the $1/p_{\mathrm{T}}^2$ of the object, clustering the high p_{T} objects first. This procedure leads to a circular jets.

5 Data sets and luminosity

5.1 Collider data

The data collected with minimum bias and jet triggers is used. Currently we have used Runs 132440 through 135175. The runs numbers and the luminosity sections analyzed are given in

`./StreamExpress/Cert_132440-135175_7TeV_StreamExpress_Collisions10_JSON.txt`.

These data correspond to ~ 10 nb^{-1}.

The events are required to pass bit 40 or bit 41. In addition, the event is required to be in-time with beam crossing by requiring the BPTX bit to be set. The events which pass any of the Beam

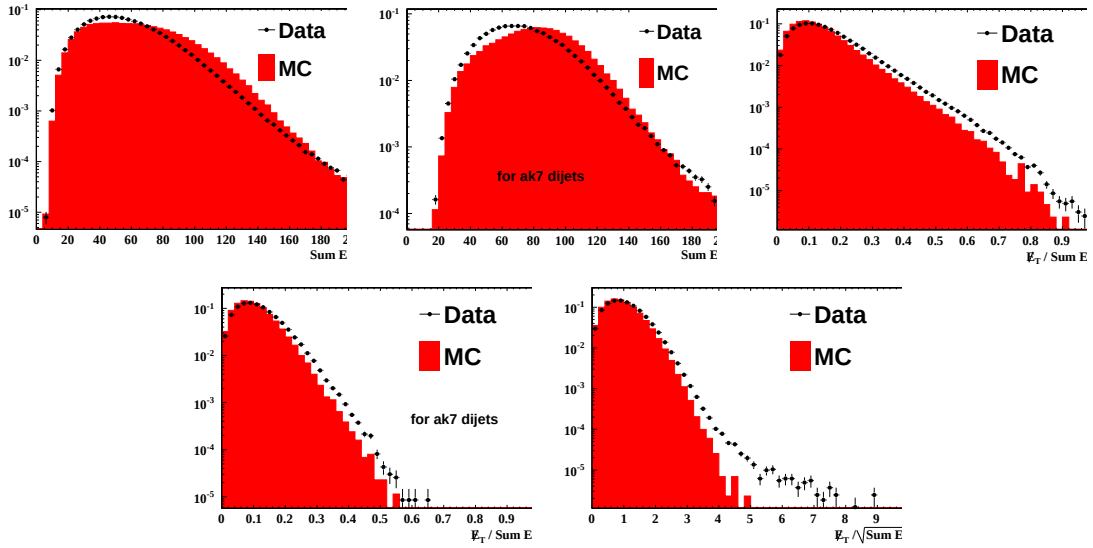

Figure 7: $\not\!\!E_T$, $\not\!\!E_T/\sum E_T$and $\not\!\!E_T$ significance $\not\!\!E_T/\sqrt{\sum E_T}$ distributions in the data

Halo triggers labeled by bits 36,37, 38, 39 are rejected. These halo rejection and timing requirements remove most of the non-physics background from the data. In addition, the "Monster events" were explicitly removed. These monster events have high track multiplicity which are related with the beam but not with the pp collisions close to the center of detector. Events were required to have at least one good primary vertex vertex. The vertex selection cuts are given in Section 6.3.

The data sets used in this analysis are:

dataset	Name (RECO)	events	L
Data	May6		

5.2 Monte Carlo data

For QCD predictions we used PYTHIA event generator. Various data sets used are given below.

dataset	Name (GEN-SIM-RECO)	Cross section	Effective L
PYTHIA	April		
Herwig	July		

6 Analysis

6.1 Software

We use CMSSW version 3.6.1 to make the user format root-tuples. The software to create and analyze the ntuples is available at `./UserCode/KHatakeyama/JetShapeAnalyzer/`.

6.2 Missing E_T Significance

Figure 7 shows the distribution for $\not\!\!E_T/\sum E_T$in data compared to minimum bias data.

6.3 Vertex Selection Criteria

We follow the CMS recommendations and use following cuts

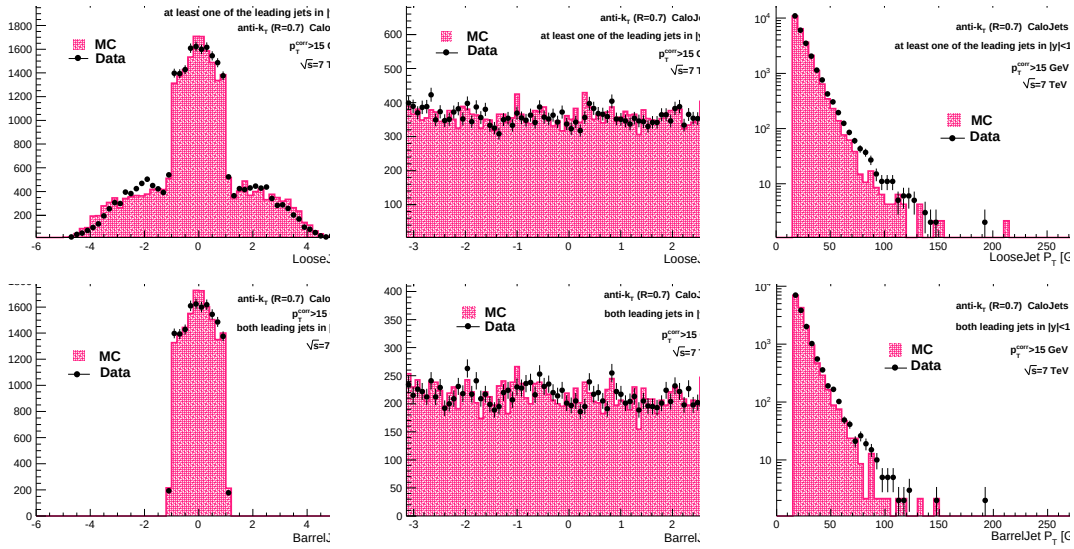

Figure 8: y, ϕ and p_{T} distributions of the selected jets.

Number of degrees of freedom	ndof >5
z position of the vertex	$\lvert z\rvert < 15$ cm
Radial position of the vertex	$\sqrt{x^2+y^2} < 2$ cm

6.4 Jet Quality Requirements (Loose JetID)

Energy fraction observed in EM calorimeter	$emf > 0.01$ if the $\lvert\eta^{\mathrm{Jet}}\rvert < 2.6$
Number of hits containing $\geq 90\%$ of the jet energy	n90Hits> 2
Fraction of the jet energy contained in a single HPD	fHPD < 0.98

6.5 Track Selection

We use For tracking study we use high quality tracks. In addition we require that reach track has at least six valid hits (nValidHits$\geq$ 6). We use track with $p_{\mathrm{T}} \geq 0.5$ GeV.

High purity tracks	Yes
p_{T}	$\geq$ 0.5? GeV
nValidHits	≥ 6
$\sigma(p_{\mathrm{T}})/p_{\mathrm{T}}$	≤ 5 (used)
$(z - z_{vertex})/\sqrt{\sigma_z^2 + \sigma_{z_{vertex}}^2}$	≤ 5 (need to add)
$(d - d_{vertex})/\sqrt{\sigma_d^2 + \sigma_{d_{vertex}}^2}$	≤ 5 (need to add)

6.6 Towers Selection

To calculate the jetshapes, we used calorimeter towers with $p_{\mathrm{T}} > 0.3$ GeV. The towers are constructed from electromagnetic calorimeter cells (crystals) and hadron calorimeter cells using Scheme 6 thresholds. In this scheme hadron calorimeter cell with energy $> 0.xx$ GeV are included. For EM calorimeter crystals, each crystal is required to have energy above 0.090 GeV and sum of 25 crystals contributing to a tower must be above **0.2** GeV. The ECAL crystals are readout using a selective readout scheme.

Figure 9: Number of particles with $R = 0.7$ of the jet axis in bins of p_{T} of the jet in PYTHIA MC QCD multijet events

Figure 10: The p_{T} distribution of the stable particles in a jet for different jet p_{T} bins in PYTHIA Monte Carlo events.

7 Multiplicity of Jet Constituents

FiguresJune4 9, 13 and 14 present the multiplicity distributions for particles, calorimeter towers and tracks in a jet, respectively, in selected p_{T} bins. The data are compared with the MC predictions and shows a good agreement.

Figure 15 summarizes the mean multiplicities of particles, tracks and calorimeter towers in a jet as a function of jet p_{T}. As expected, they increase logarithmically with increasing jet p_{T}.

8 p_T Distributions of Particles, Tracks and Towers in a Jet

p_{T} distributions of particles, tracks and towers in a jet are shown in FiguresJune4 10, 17 and 16, respectively. These distributions become harder with increasing jet p_{T}.

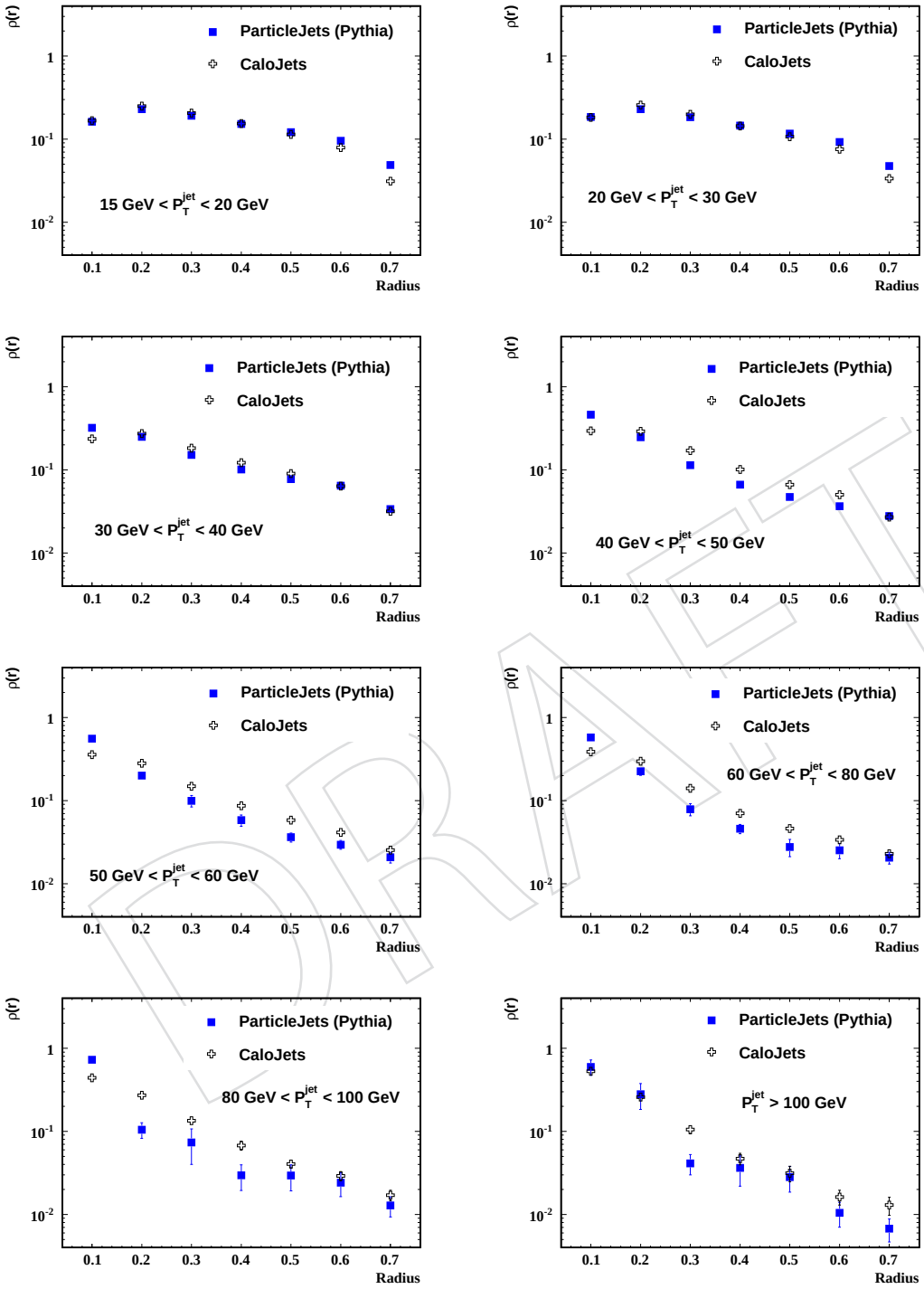

Figure 11: Particle differential jetshapes and calorimeter differential jetsshapes in PYTHIA MC events in bins of p_T at $\sqrt{s} = 7$

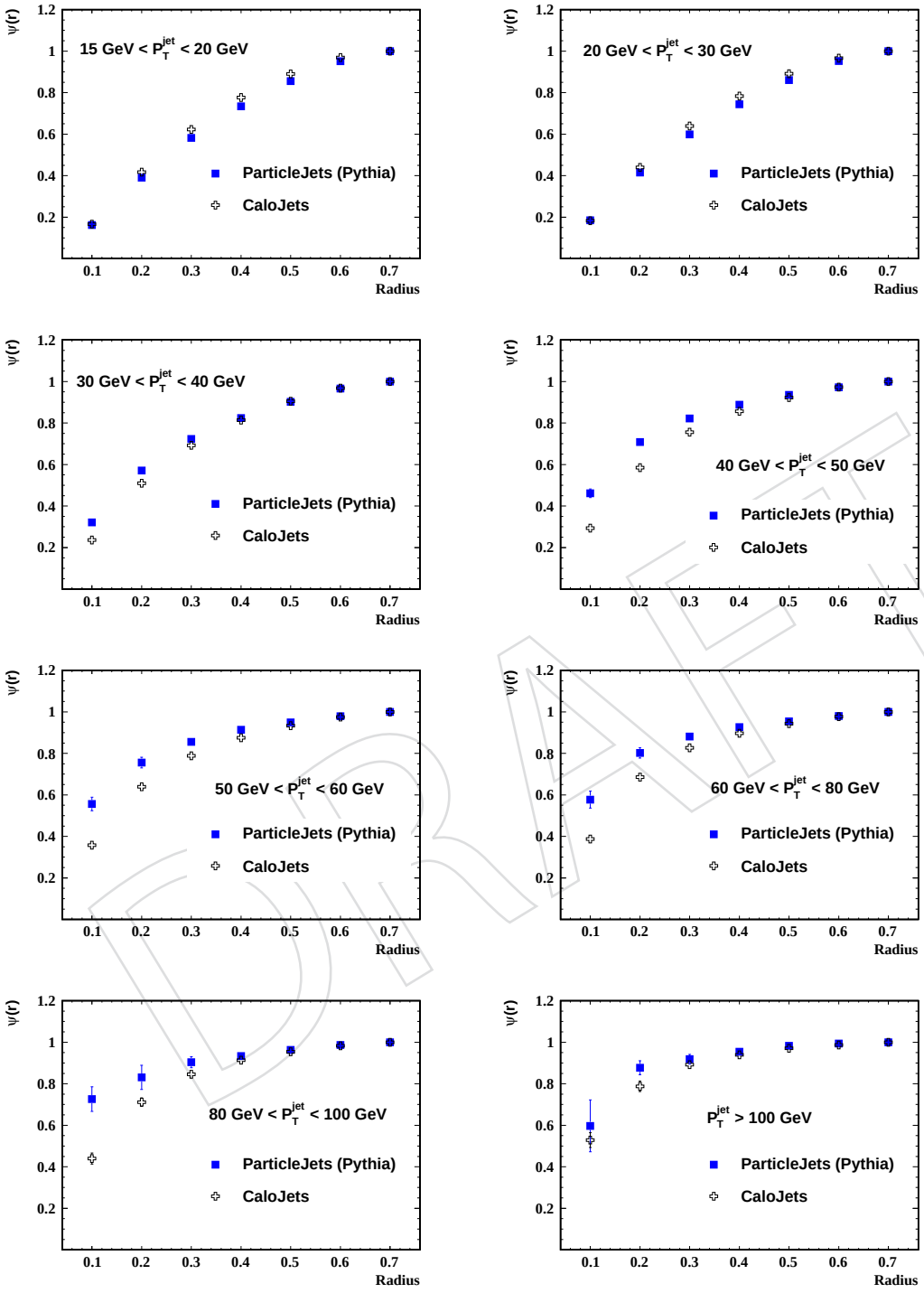

Figure 12: Particle integarated jetshapes and calorimeter integrated jetsshapes in PYTHIA MC events in bins of p_T at $\sqrt{s} = 7$

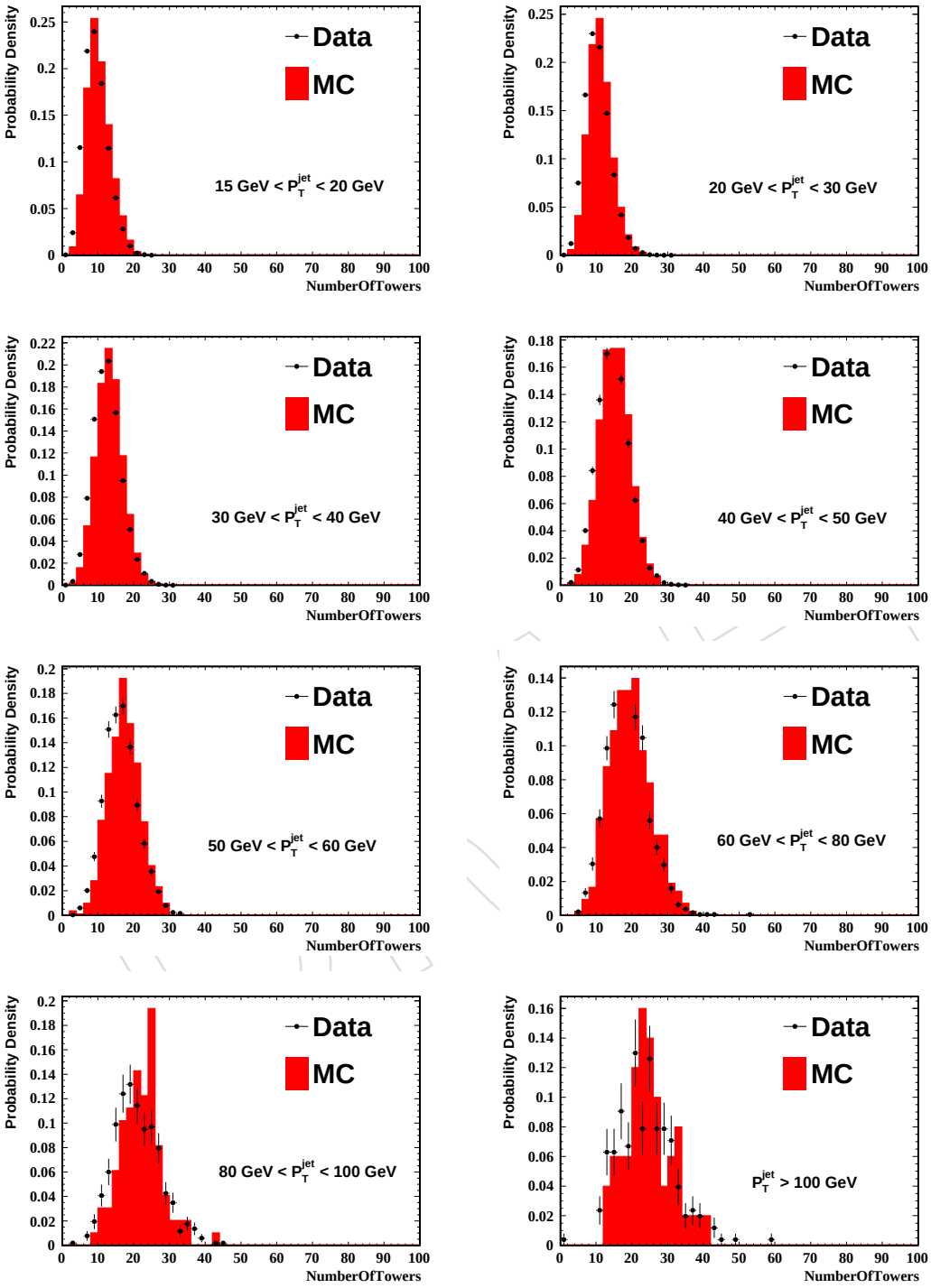

Figure 13: Number of towers with $R = 0.7$ of the jet axis in bins of p_{T} of the jet in CMS data at $\sqrt{s} = 7$

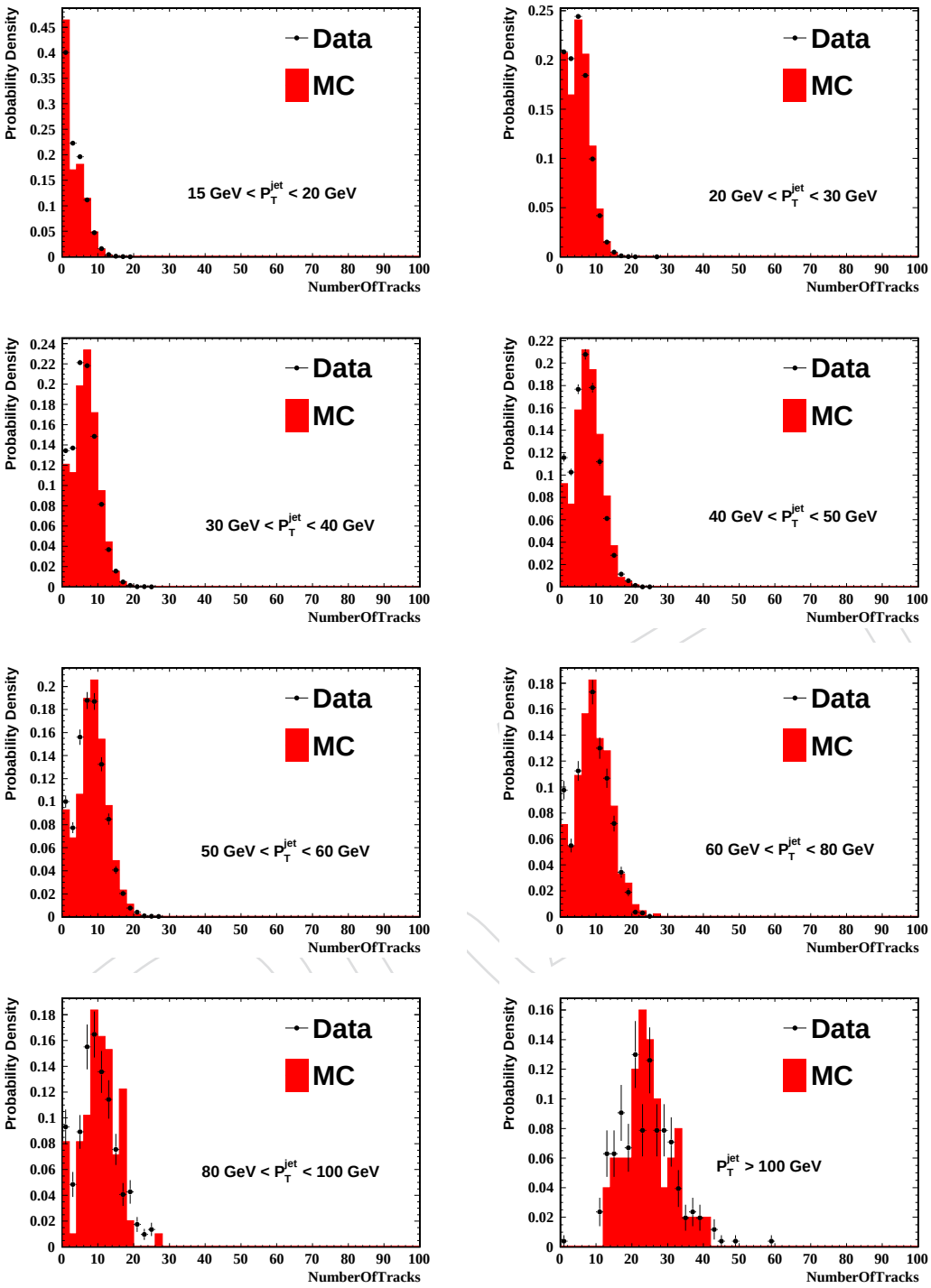

Figure 14: Number of good tracks with $R = 0.7$ of the jet axis in bins of p_{T} of the jet in CMS data at $\sqrt{s} = 7$

Figure 15: Number of towers, tracks in a jets as a function of jet p_{T}.

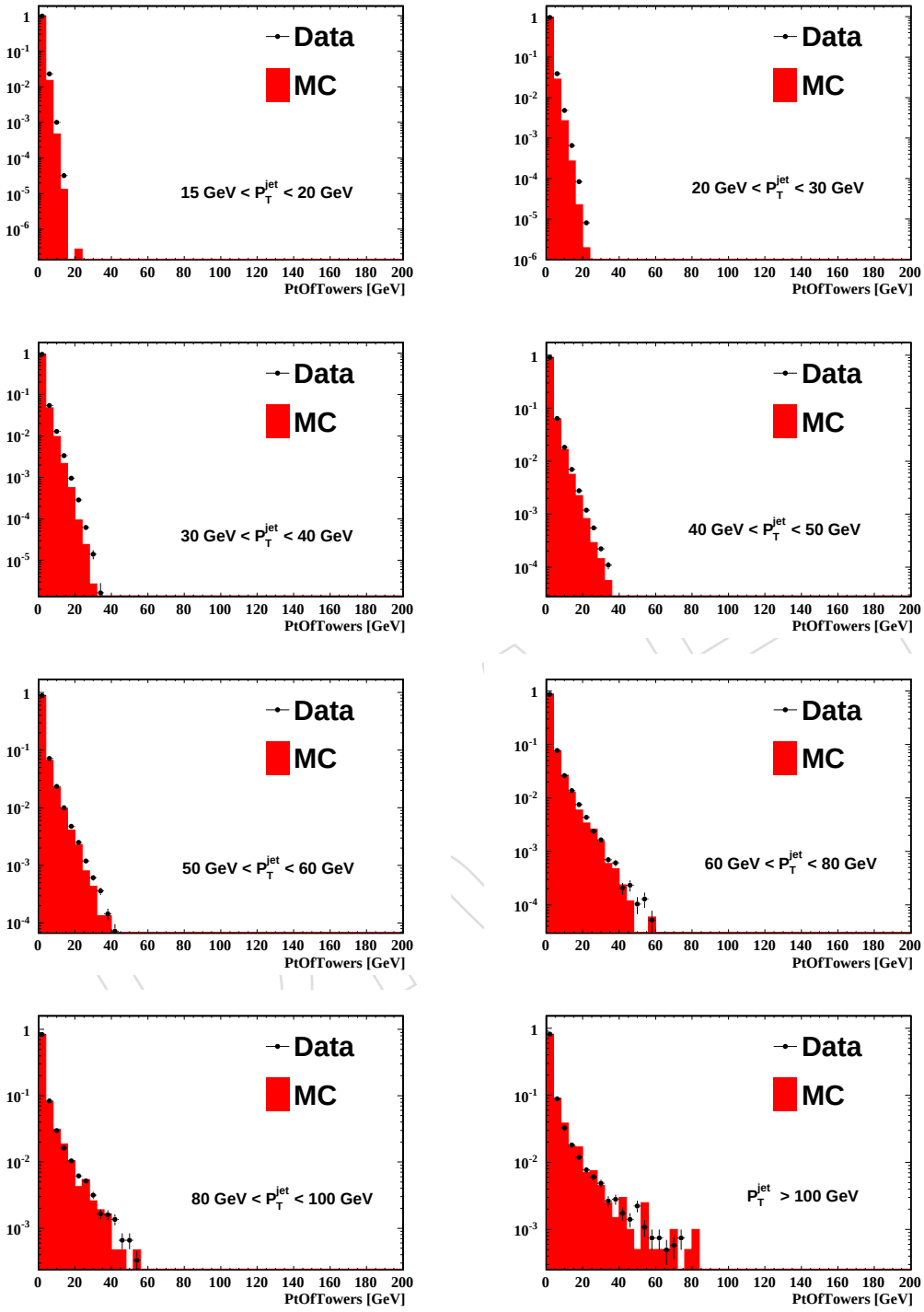

Figure 16: The p_{T} distribution of the towers in a jet for different jet p_{T} bins. The data are compared to the MC predictions.

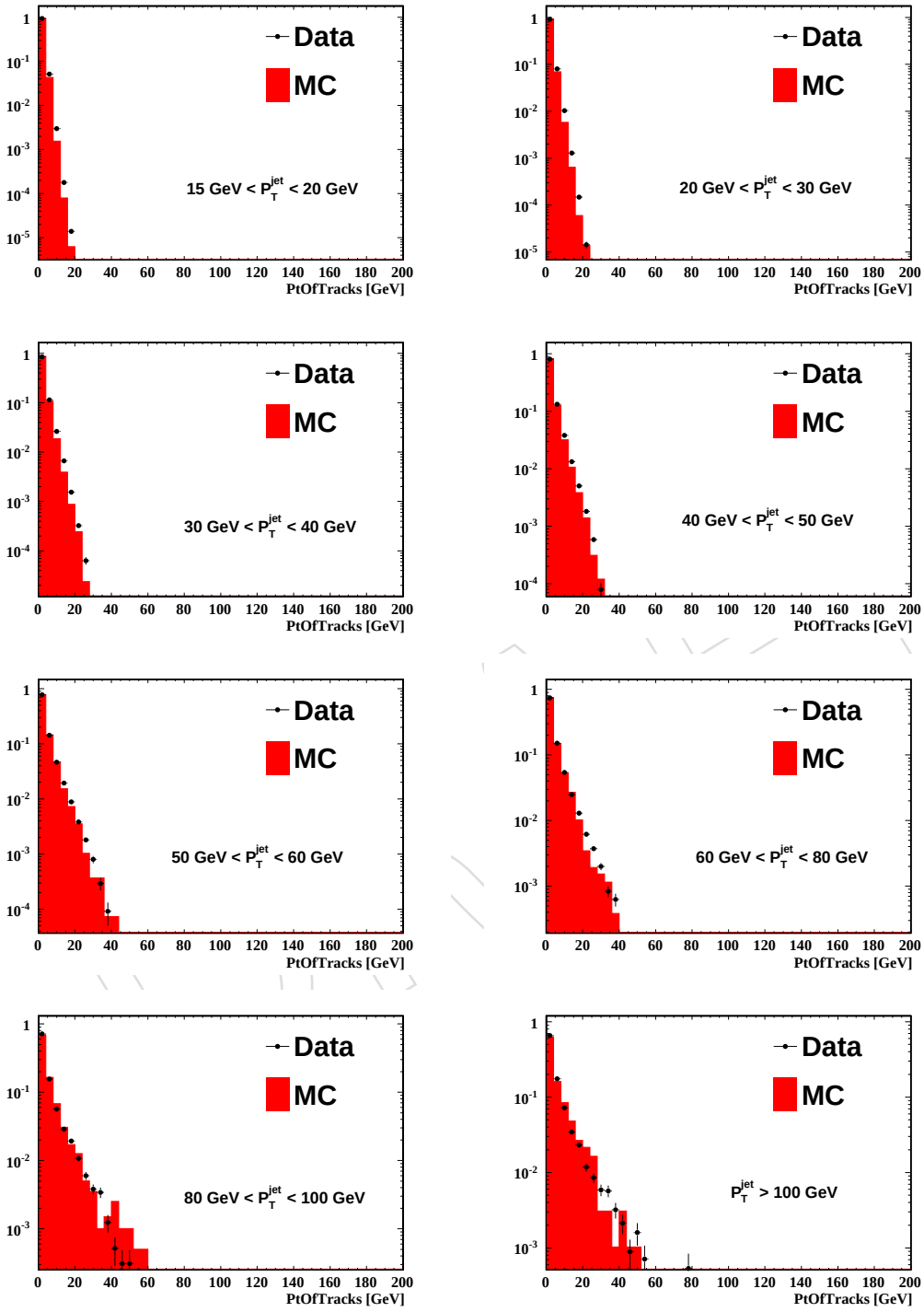

Figure 17: The p_{T} distribution of the tracks in a jet for different jet p_{T} bins. The data are compared to the MC predictions.

9 Raw Jet Shapes

Figure 20 and Figure 21 show the differential and integrated jet shapes for data events measured using calorimeter towers for various jet p_T bins. Most of the momentum is concentrated within a small region around the jet axis. Jet shapes become narrower with the increasing p_T of the jet. The data are in good agreement with the calorimeter jetshapes predicted by PYTHIA event generator using underlying event tune DW. The jetshapes measured using tracks is also shown for both data and simulated events and show good agreement. The jetshapes measured using tracks also show the the same trend, though they are slightly wider.

10 Jet Shape Corrections

Due to various detector effects, the measured (calorimeter) jet shapes are different than the true (particle) jet shapes. Due to the magnetic field of CMS, charged particles with $p_T < 0.9$ GeV do not reach the calorimeter. In addition showers from particles interacting with the detector material spread their energy over many calorimeter towers. The measured jet shapes must be corrected for these detector effects. Correction factors were determined as a function of distance from the jet axis using MC events before and after the CMS detector simulation. For this approach to be valid, the MC simulation must describe the calorimeter response accurately. Currents studies of the single particle response show that the data are well described by the data [14]. The jetshape corrections have been determined using unmatched jets and are applied as a function of distance from the jet axis.

The correction factors $C_D(r)$ and $C_I(r)$ for differential and integrated jet shapes are defined in Equations 5 and 6, respectively:

$$C_D(r) = \rho_{MC}^{PARTICLE}(r)/\rho_{MC}^{CAL}(r) \tag{6}$$

$$C_I(r) = \psi_{MC}^{PARTICLE}(r)/\psi_{MC}^{CAL}(r) \tag{7}$$

where calorimeter towers and generated particles have been used to reconstruct differential $\rho_{MC}^{CAL}(r)$, $\rho_{MC}^{PARTICLE}(r)$ and integrated jet shapes $\psi_{MC}^{CAL}(r)$, $\psi_{MC}^{PARTICLE}(r)$ in different bins of jet p_T.

Measured calorimeter jet shapes are then used to determine the corrected differential jet shapes $\rho^{corrected}(r) = C_D(r) \cdot \rho^{CAL}(r)$ and integrated jet shapes $\psi^{corrected}(r) = C_I(r) \cdot \psi^{CAL}(r)$.

The correction factors $C_D(r)$ in Figure 24 do not show a significant dependence on jet p_T in the region $r < 0.5$. They vary between 0.6 and 1.3 as a function of r, and between**1.3-2** for the region $r > 0.5$. The correction factors for integrated jet shapes in Figure 25 vary from **0.9 to 1.06** for all radius and p_T bins. For the integrated distributions, the correction factors do not have a strong dependence on jet p_T.

11 Corrected Jet Shapes

The corrected differential and integrated jet shapes are shown in FiguresJune4 26 and 27. Close to the jet axis, the jet shape is dominated by collinear gluon emission, whereas at large distance from the jet axis, the jet shape reflects large angle gluon emissions, which can be calculated perturbatively. The jet shape $\psi(r)$ increases faster with r for jets at larger p_T indicating that these jets are more collimated.

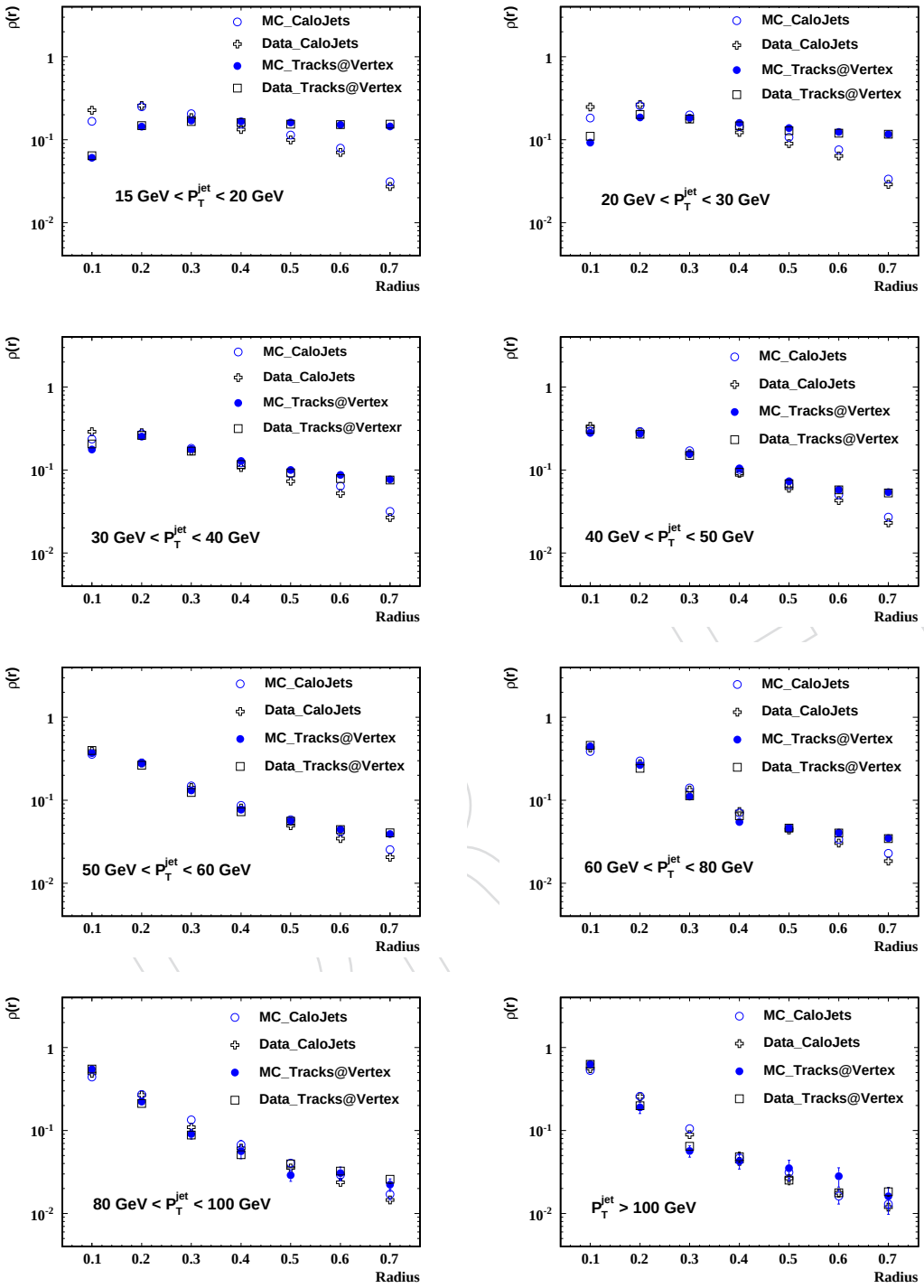

Figure 18: Differential jetshpes for jet in various $p_{\mathrm{T}}^{\mathrm{Jet}}$ bins. The data are compared with PYTHIA predictions for both calorimeter jetshapes and track jetshapes. The track jetshapes are measured at the vertex.

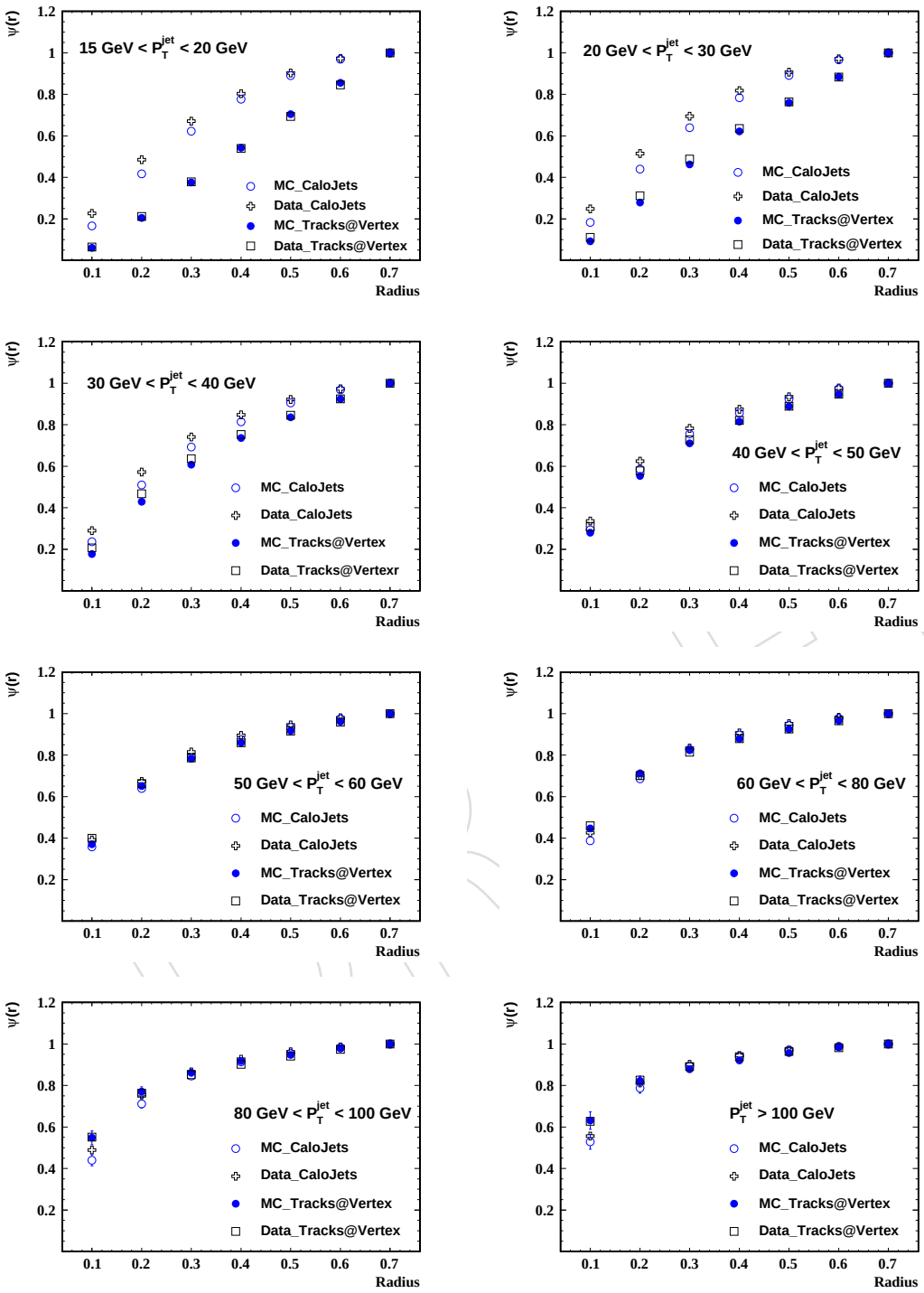

Figure 19: Integrated jetshpes for jet in various $p_{\mathrm{T}}^{\mathrm{Jet}}$ bins. The data are compared with PYTHIA predictions for both calorimeter jetshapes and track jetshapes. The track jetshapes are measured at the vertex.

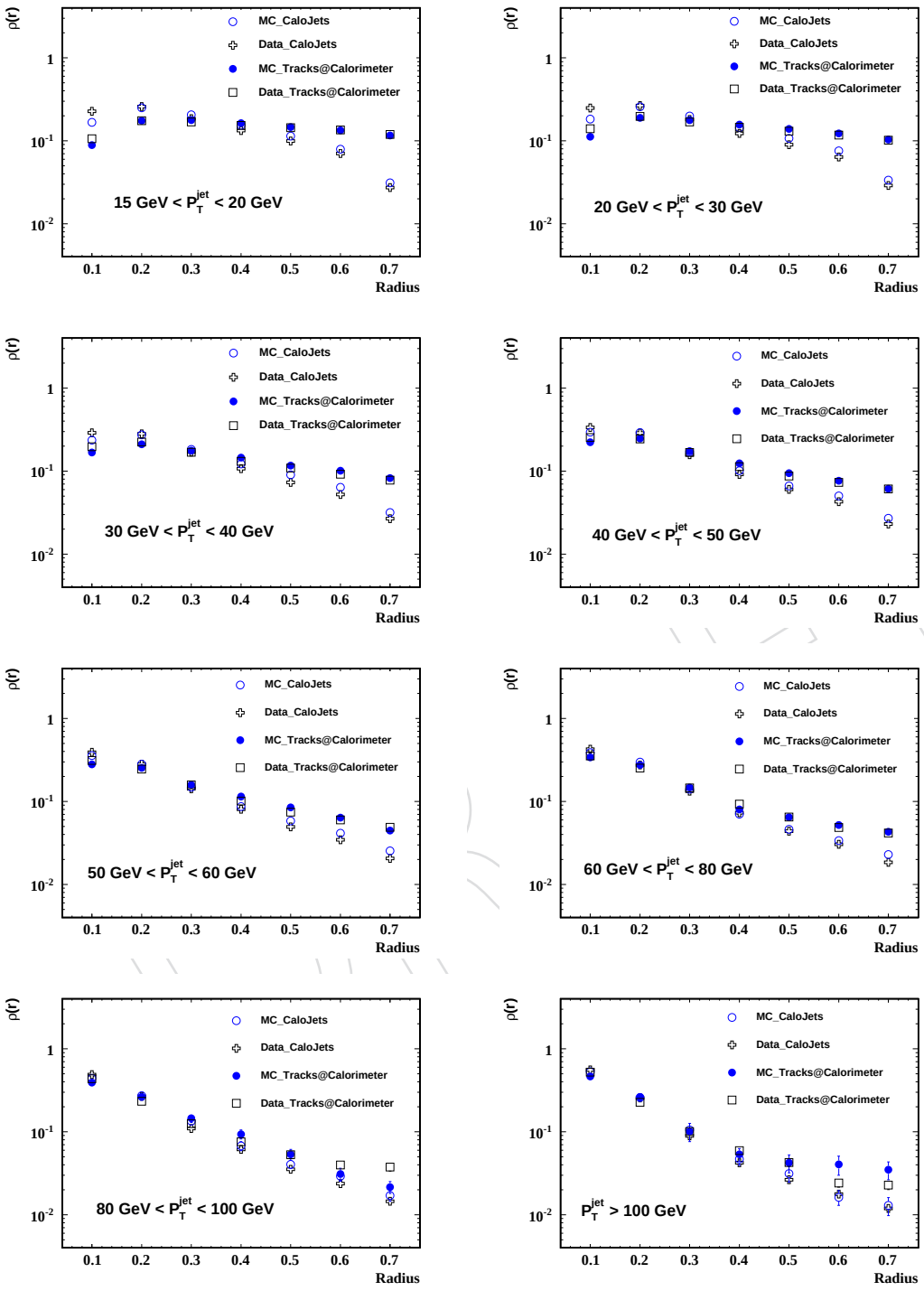

Figure 20: Differential jetshpes for jet in various $p_{\mathrm{T}}^{\mathrm{Jet}}$ bins. The data are compared with PYTHIA predictions for both calorimeter jetshapes and track jetshapes. The track jetshapes are measured after propogating the tracks to calorimeter surface.

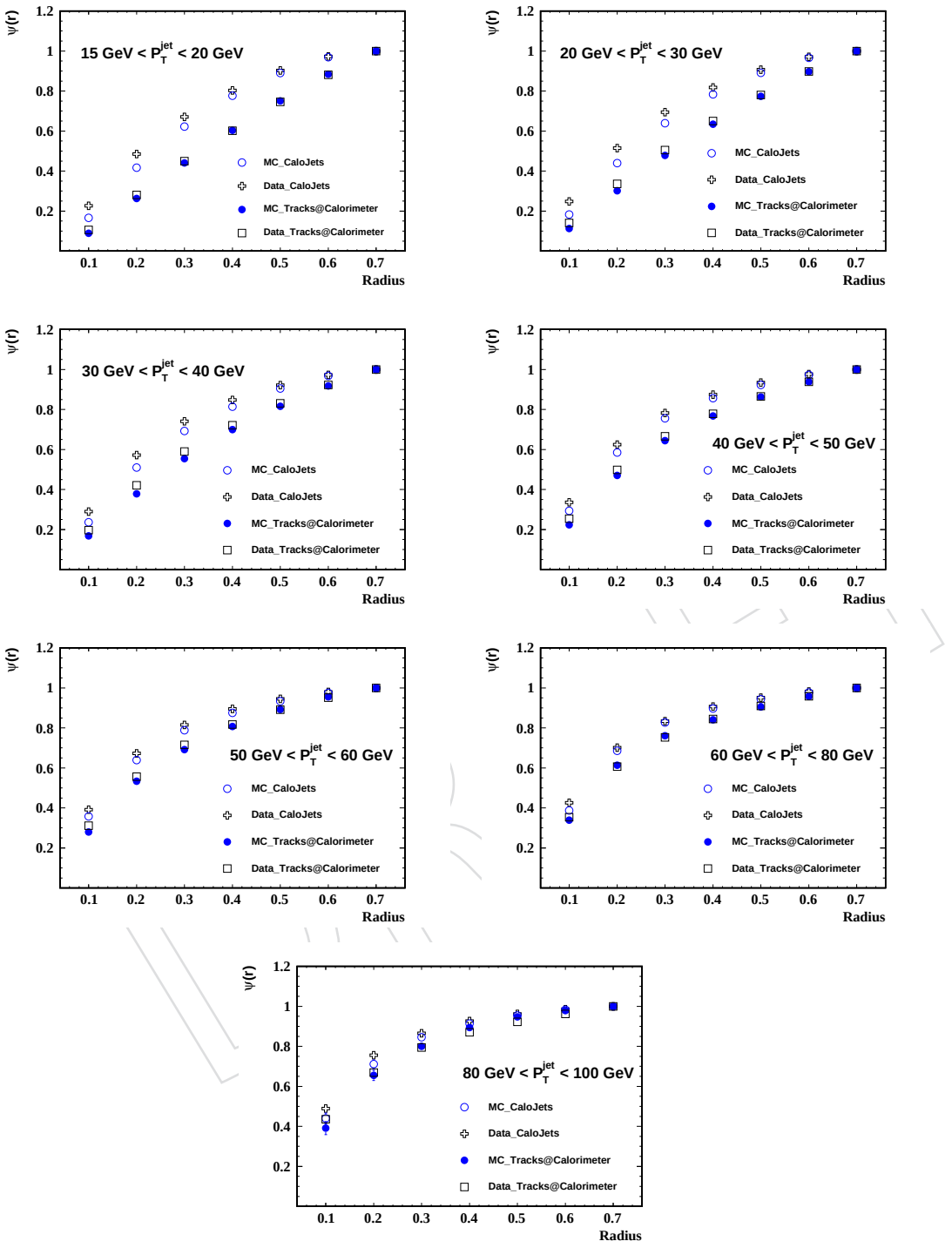

Figure 21: Integrated jetshpes for jet in various $p_{\mathrm{T}}^{\mathrm{Jet}}$ bins. The data are compared with PYTHIA predictions for both calorimeter jetshapes and track jetshapes. The track jetshapes are measured after propogating the tracks to calorimeter surface.

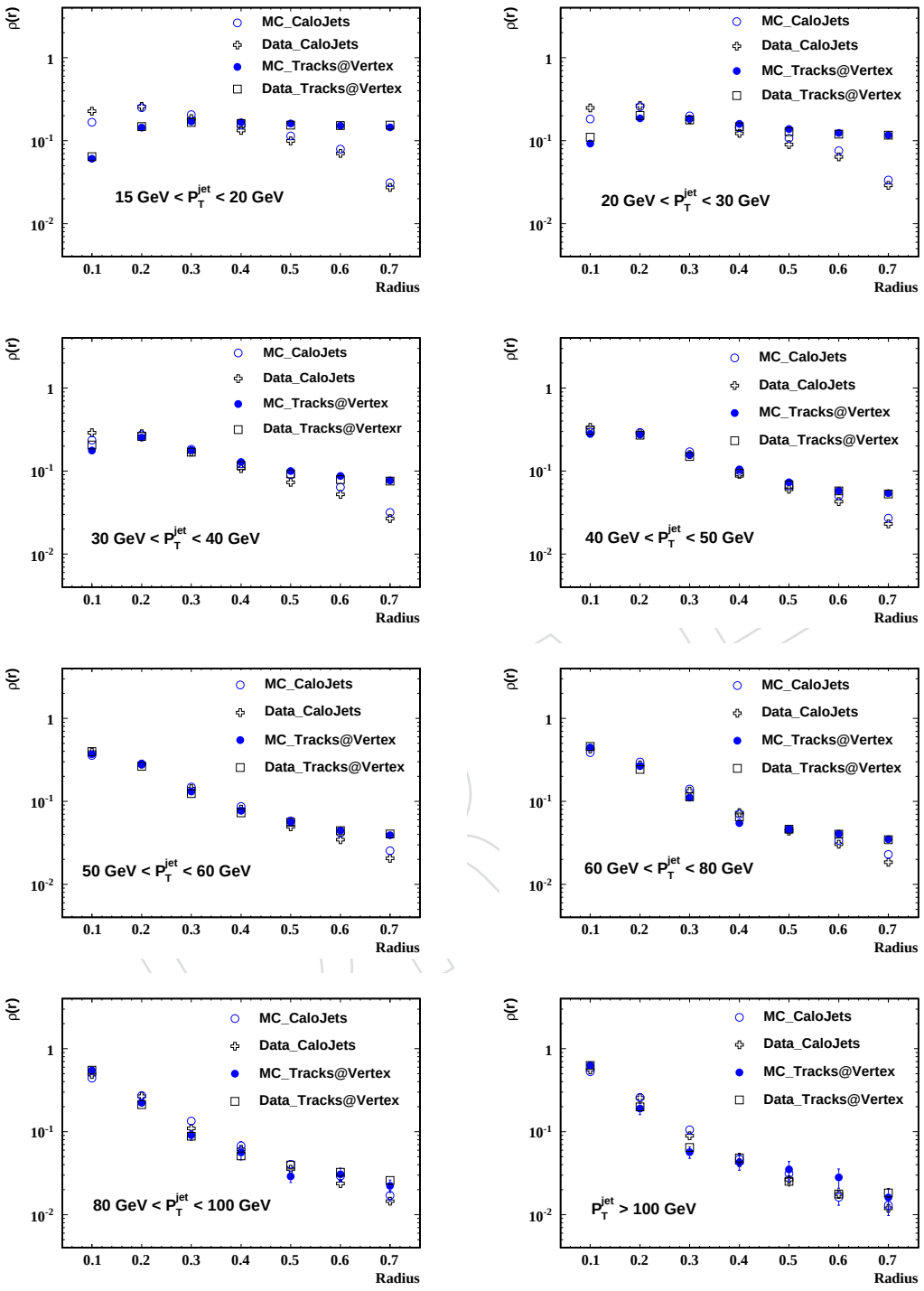

Figure 22: Differential jetshpes for jet in various $p_{\mathrm{T}}^{\mathrm{Jet}}$ bins. The data are compared with PYTHIA predictions for both calorimeter jetshapes and track jetshapes.

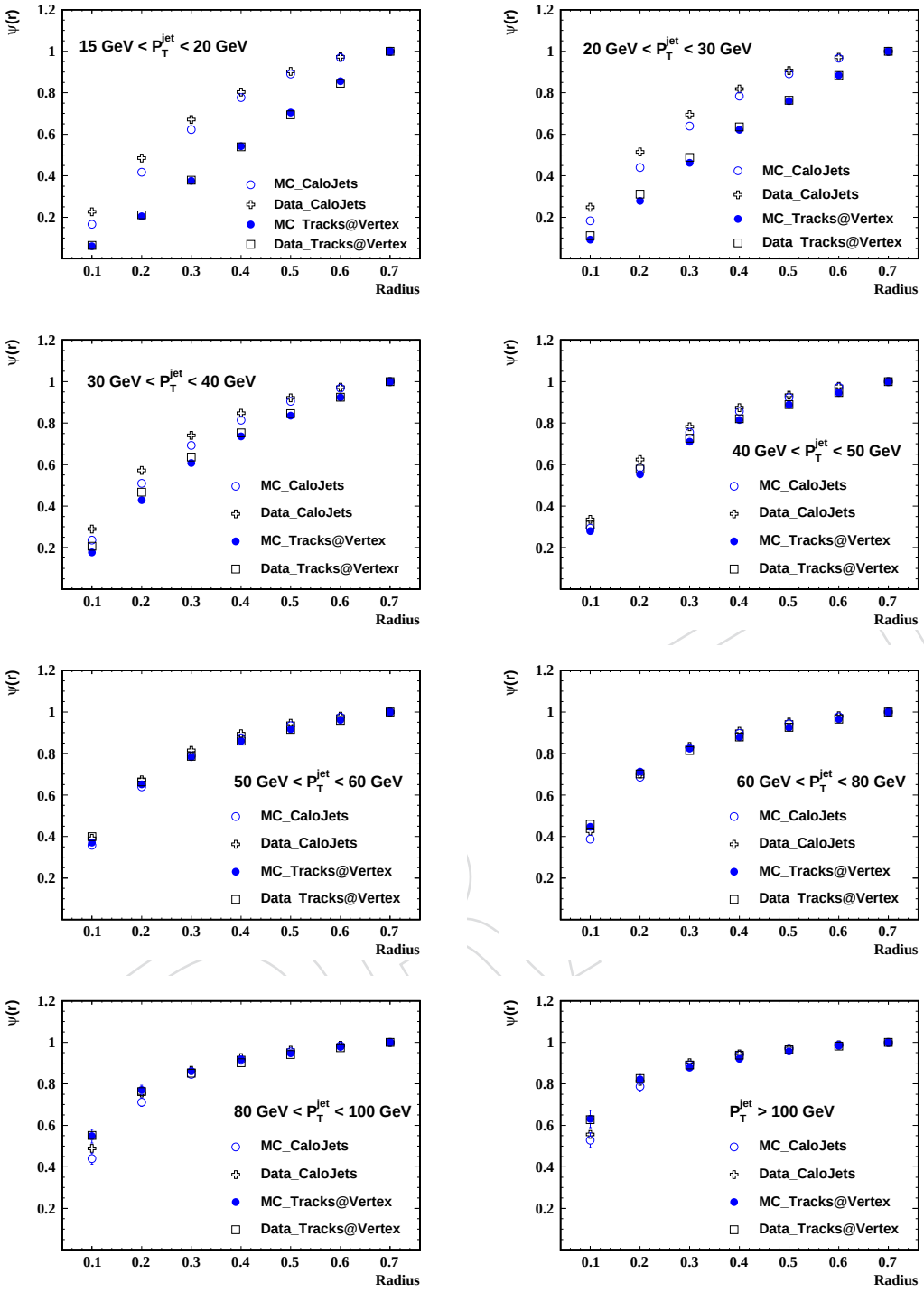

Figure 23: Integrated jetshpes for jet in various $p_{\mathrm{T}}^{\mathrm{Jet}}$ bins. The data are compared with PYTHIA predictions for both calorimeter jetshapes and track jetshapes.

Figure 24: Correction factors for differential jetshpes for jet in various $p_{\mathrm{T}}^{\mathrm{Jet}}$ bins as determined from PYTHIA MC event generator.

Figure 25: Correction factors for integrated jetshpes for jet in various $p_{\mathrm{T}}^{\mathrm{Jet}}$ bins as determined from PYTHIA MC event generator.

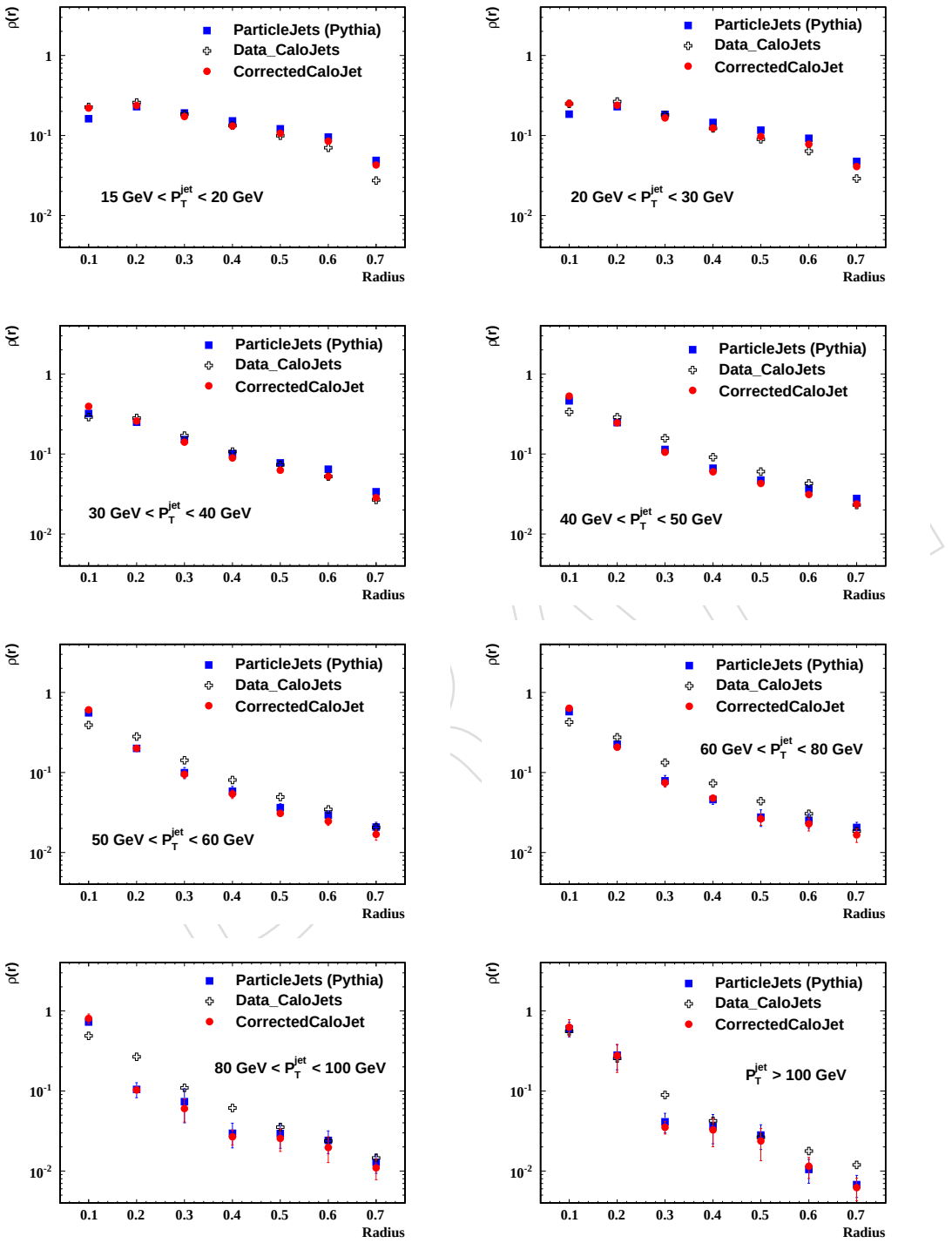

Figure 26: Particle level differential jetshpes for jet in various $p_{\mathrm{T}}^{\mathrm{Jet}}$ bins. The data are compared with PYTHIA predictions.

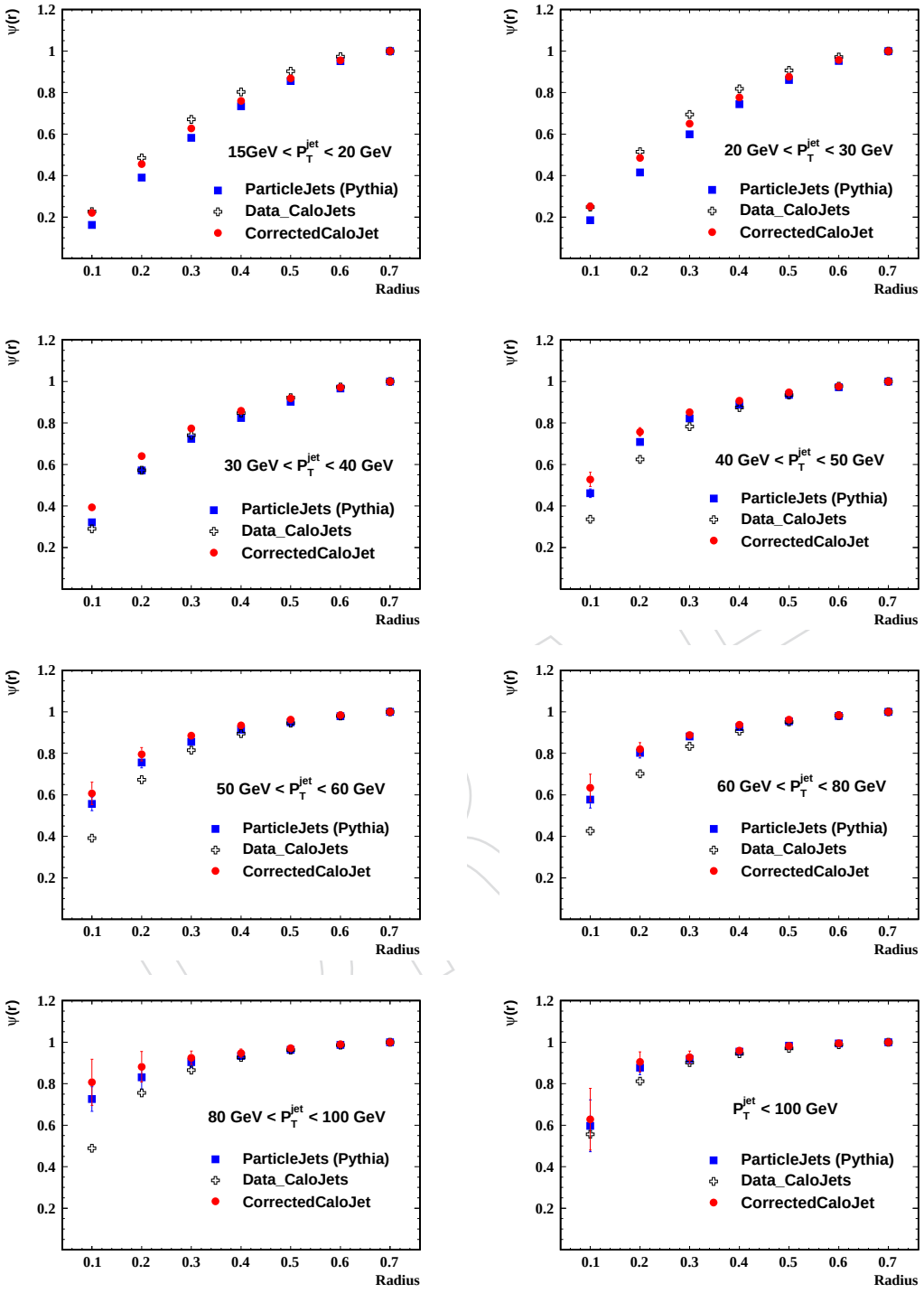

Figure 27: Particle level integrated jetshpes for jet in various $p_{\mathrm{T}}^{\mathrm{Jet}}$ bins. The data are compared with PYTHIA predictions.

12 Sensitivity of Jet Shapes to Underlying Event Tunes

The energy from the underlying event (UE) contributes to jets and impacts the jet shapes. In addition, the underlying event tuning is intrinsically related to the initial state radiation and the showering/fragmentation model. The observed jetshape distributions are compared to jetshapes predictions from PYTHIA event generator with different UE tunes and from the HERWIG event generator. All these models are consistent with Tevatron measurements at $\sqrt{s} = 1.8$ and $\sqrt{s} = 1.96$ TeV. The default CMS PYTHIA tune [15] is D6T in which parameter p_{T0} increases slowly withe the center of mass energy $\sqrt{s}$. For this tune the UA5 underlying event measurements were used. In addition, DW, Perugia-0 (P0) and Pro-QCD20 tunes are available. The DW tune has stronger energy dependence than D6T tune. For Perugia-0 (P0) and Pro-QCD20 tunes, the PYTHIA fragmentation functions have been tuned to the LEP and other measurements using Professor program before the parameters controlling the UE are adjusted. For Perugia tunes, P0 tunes p_{T}-ordered showering model is used whereas all other tunes use conventional virtuality ordering showering procedure are used. Currently, MC data using some of these tunes is available. We plan to add prediction from other PYTHIA tunes and Herwig++ event generator when they become available.

The jet shapes for PYTHIA D6T, PYTHIA DW and PYTHIA P0 are shown in Fig. 28 for the differential jet shapes and in Figure 29 for the integrated jet shapes. At low jet p_{T}, one can observe the difference in jet shapes due to the UE contribution. Underlying event contribution as a fraction of the jet p_{T} is larger at low p_{T} and at large radii. The data are better described by PYTHIA P0.

13 Quark and Gluon Jet Shapes

Jet shapes are sensitive to quark and gluon jet contributions. The quark jets are narrower than the gluon jets due to the coupling strengths for gluon emission which depend on the color factors C_F=4/3 for radiating quarks and C_A=3 for gluons. It is instructive to separate the jets by the flavor and study their shapes. As shown above in Fig 1, the flavor composition of the jets in QCD multi-jet sample changes with the transverse energy of the jets as the proton parton distribution change with momentum fraction x. Fraction of jet momentum with $r \leq 0.2$ is shown in Fig. 32. The data are compared with parton shower+hadronization MC predictions for quark and gluon jets. Tables 2, 3 and 4 provide details of the calculation of statistical and systematic uncertainties for $1 - \psi(r = 0.2)$ in all p_{T} bins. The simulated jets are classified as quark or gluon jets by matching the particle jets with a parton from $2 \rightarrow 2$ scattering within $\Delta R < 0.5$ in (y, ϕ) space. The MC predicts that the measured jet shapes are dominated by contributions from gluon initiated jets at low jet p_{T} while contributions from quark initiated jets become important at high jet p_{T}. MC also predicts that the both quark and gluon jets become narrower with increasing jet p_{T}. The data are in qualitative agreement with these predictions.

14 Systematic Uncertainties

The main sources of systematic uncertainties include:

- Jet energy scale
- Transverse shape of calorimeter showers
- Non-linearity of calorimeter response
- Jet fragmentation

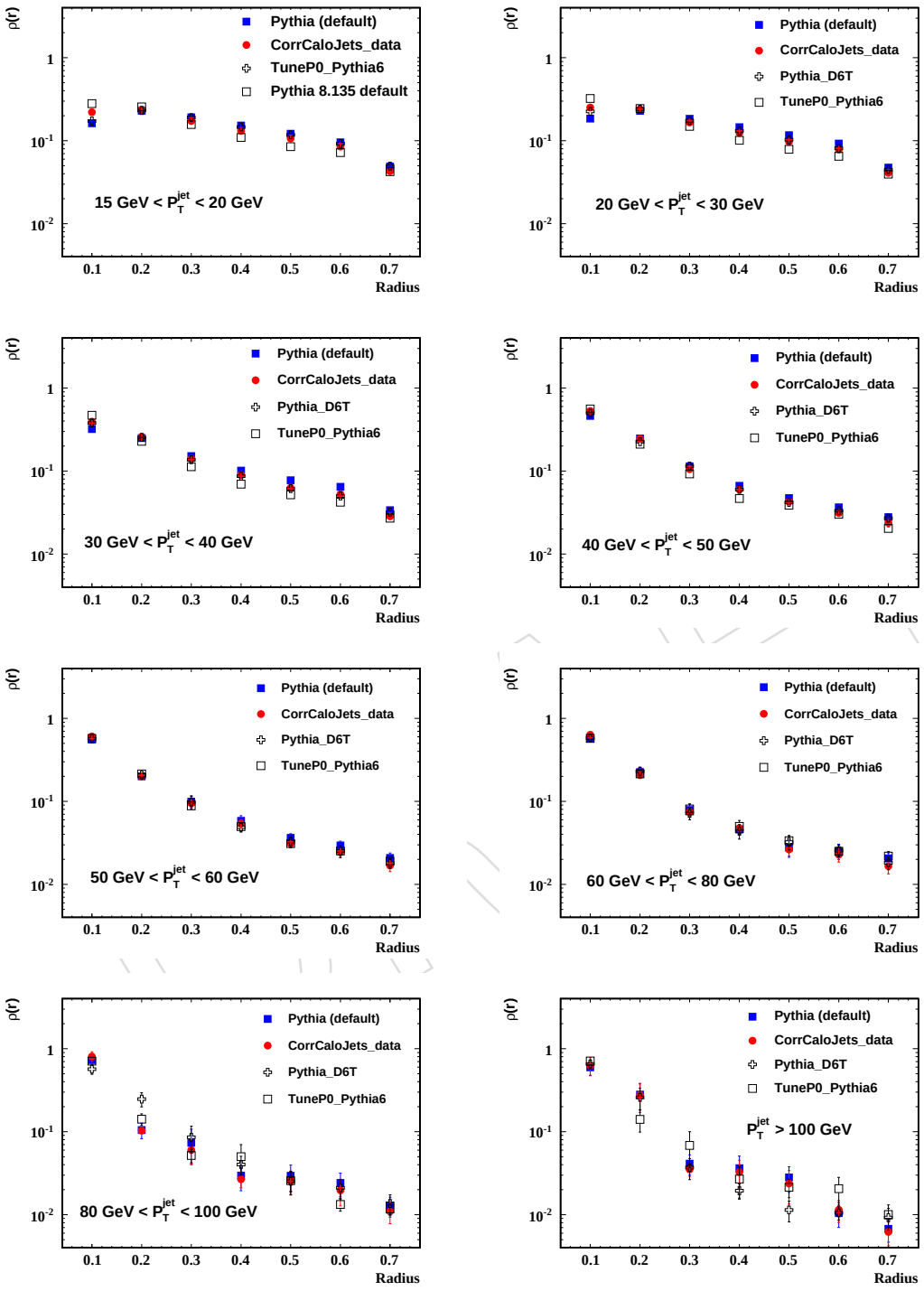

Figure 28: Differential jetshpes for jet in various $p_{\mathrm{T}}^{\mathrm{Jet}}$ bins compared to PYTHIA MC predictions using different UE tunes

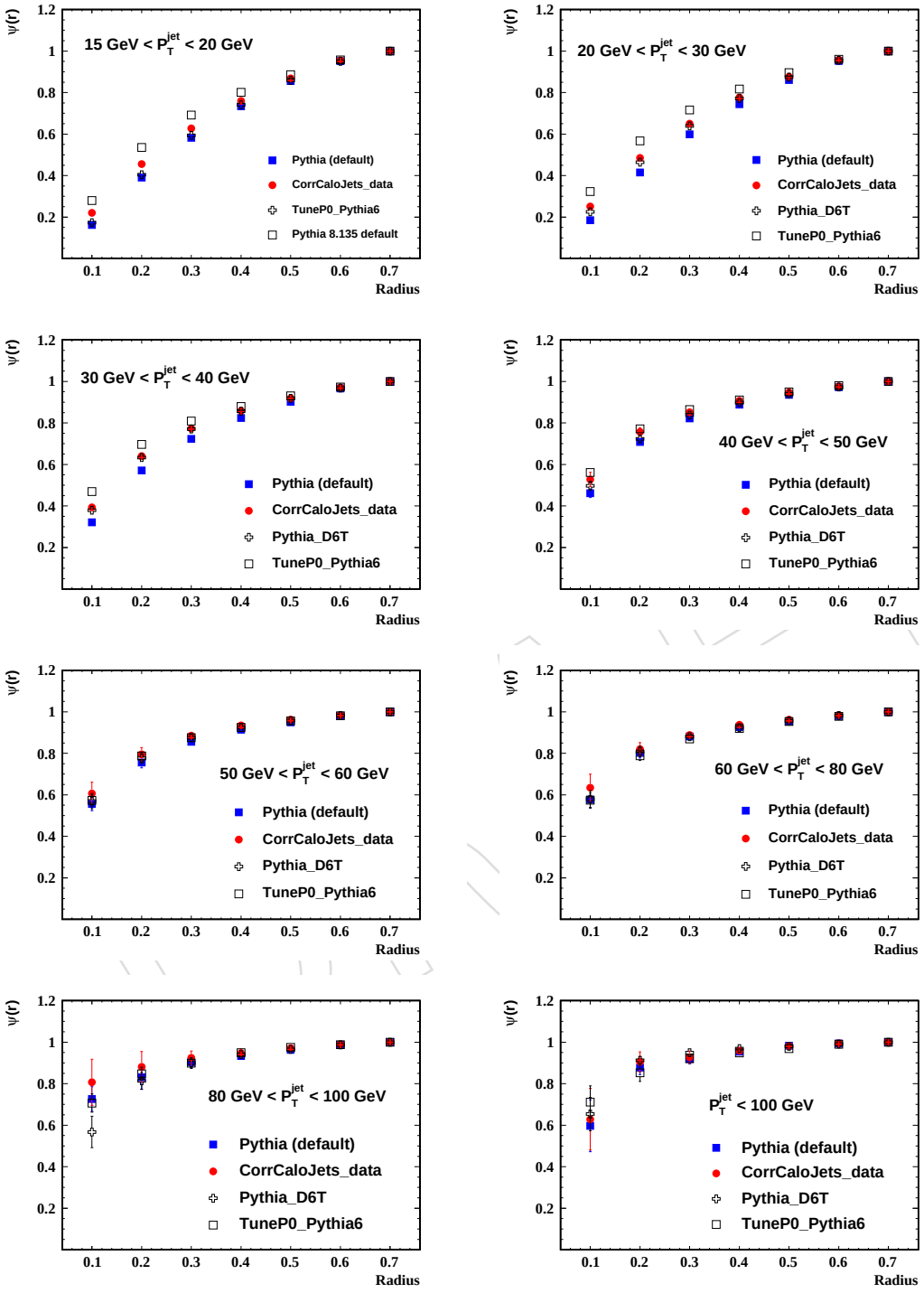

Figure 29: Integrated jetshpes for jet in various $p_{\mathrm{T}}^{\mathrm{Jet}}$ bins compared to PYTHIA MC predictions using different UE tunes

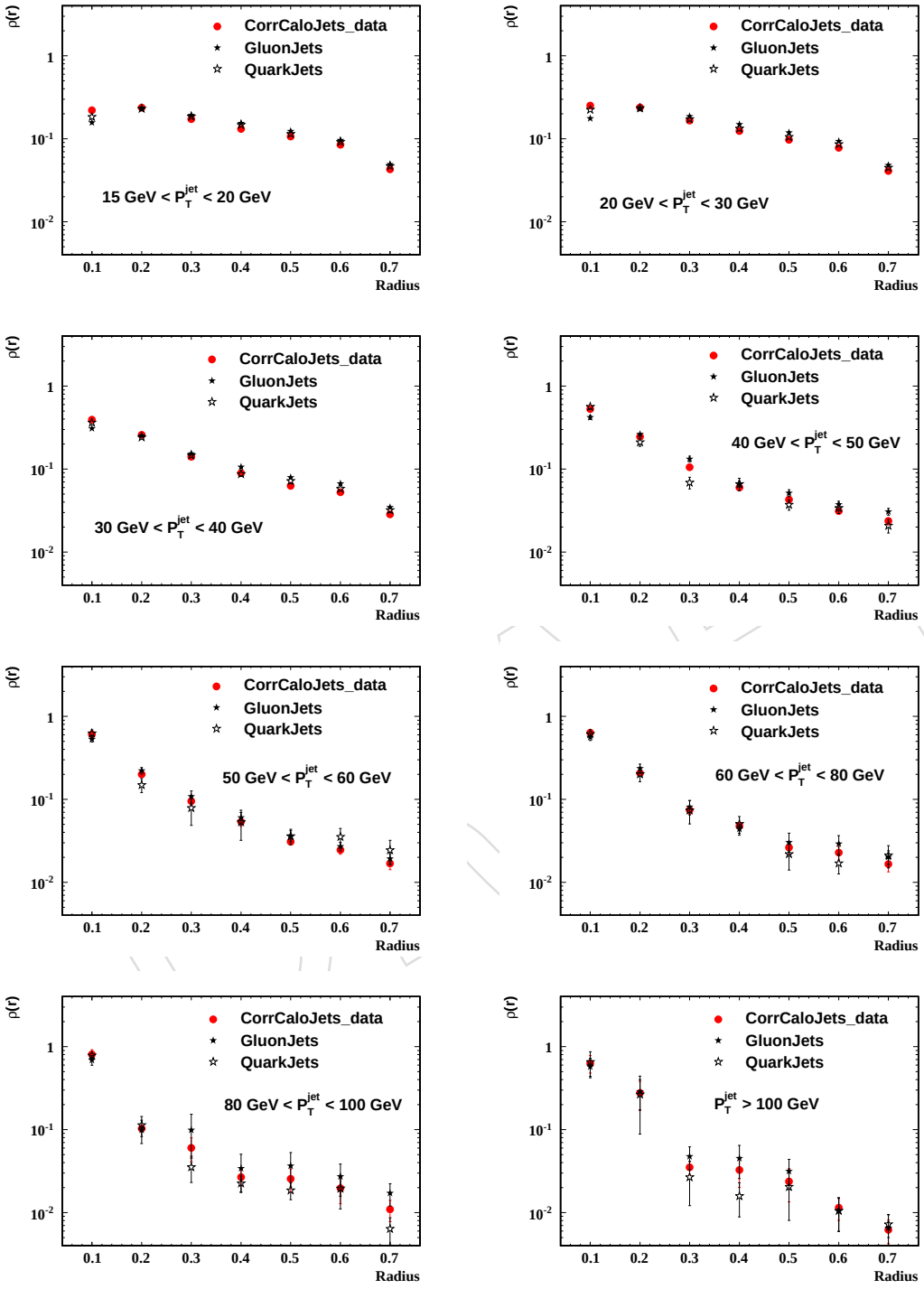

Figure 30: Measured integrated jetshapes compared to quark and gluon jetshapes from Pythia.

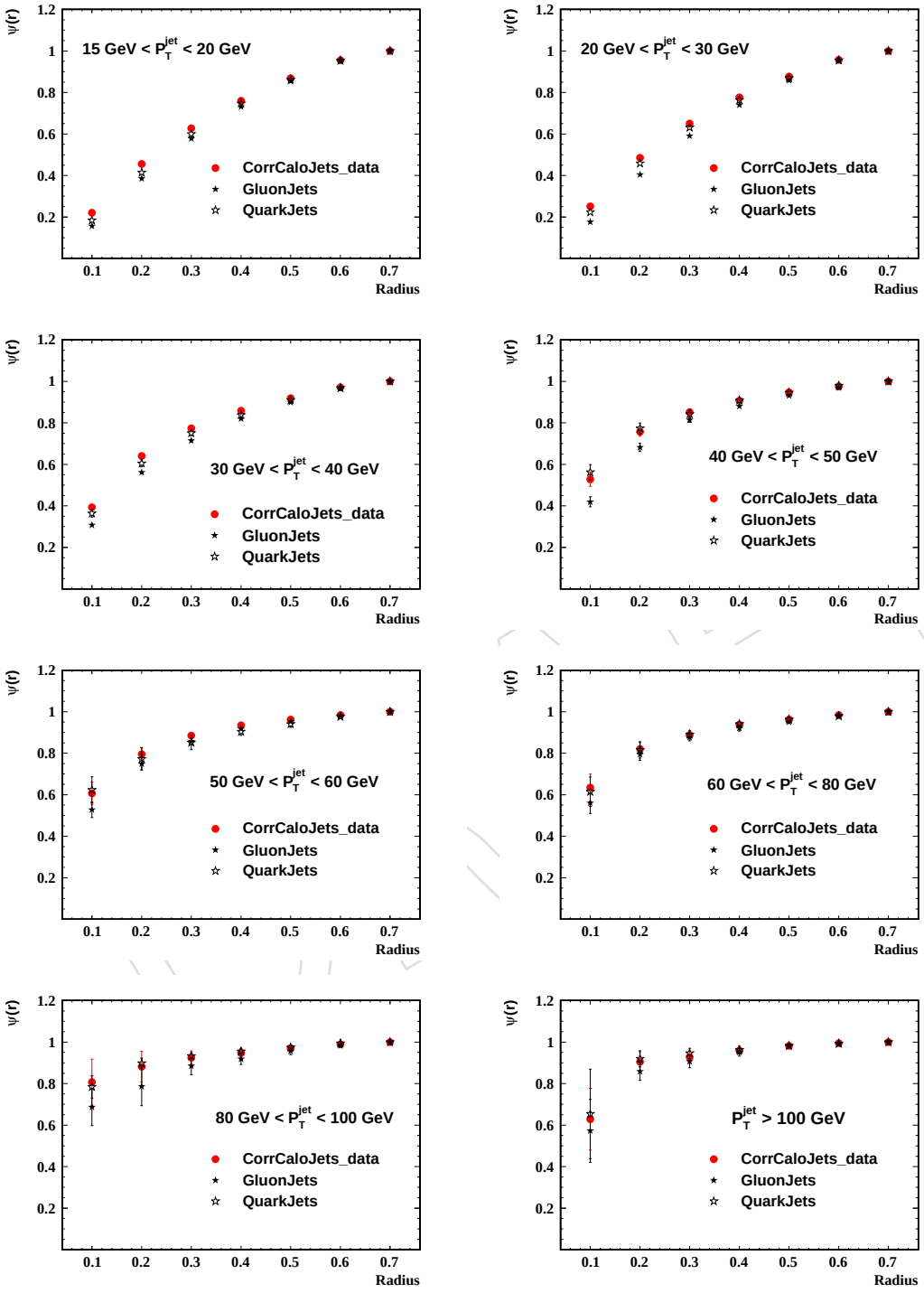

Figure 31: Measured integrated jetshapes compared to quark and gluon jetshapes from Pythia.

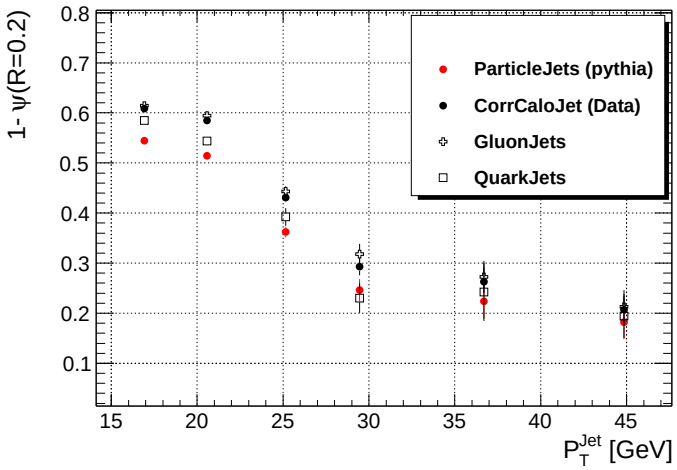

Figure 32: Jet transverse momentum fraction outside r=0.2 regions.

The uncertainties arising from jet energy and position resolution, and from event selection cuts are expected to be negligible compared to the sources listed above and are not considered.

14.1 Jet Energy Scale

Current expectation of the JES uncertainty at start up is $\pm$10% [16]. Changing the JES correction within its uncertainty changes the jet shapes as jets migrate between p_{T} bins. Jet shapes vary slowly with jet p_{T} and thus this effect is expected to be small. To determine the impact on the jet shapes, we changed the p_{T} of the jet by $\pm$10% and repeated the whole analysis. The comparison between the default JES corrections and the modified corrections is shown in Figure 33. The corresponding systematic uncertainties on the differential jet shape are 10% at r=0.1 and $<$ 5% at r =0.2 for all jet p_{T}. At larger $r \geq 0.5$ they are $<$ 20%.

The uncertainties on the integrated jet shape are 10% at r=0.1, 5% at r=0.2 for p_{T} <100 GeV, and decrease as a function of r. They are $<$ 2% at r=0.1 for $p_{\mathrm{T}} > 100$ GeV and negligible at r >0.1, as shown in Figure 35. The systematic uncertainty at r=0.7 is 0 by definition of the integrated jet shape.

14.2 Jet Fragmentation

Because the calorimeter response depends on the momenta of the particles in the jets, modeling of jet fragmentation contributes to the uncertainty on the corrected jet shapes. Uncertainties due to the fragmentation model can be estimated by comparing the correction factors determined using PYTHIA and HERWIG events.. The model of the underlying event used in HERWIG++ is described in [17]. Particle level differential and integrated jet shapes in PYTHIA DWT and HERWIG++ 2.2 [18] are shown in Figure 37 and Figure 38. Their observed difference is less than 5% at r <0.3. To determine the systematic uncertainty due to modeling of jet fragmentation we compared PYTHIA DWT and HERWIG++ differential jet shape correction factors, shown in Figure 39. They agree to $<$ 10% for $r \leq 0.2$, however, the differences can be as large as $30-40$% at $r \geq 0.5$. Note that the jet energy fraction at large r is small, which makes uncertainties on the differential jet shape measurement large in this region.

Comparisons of the integrated jet shape correction factors for PYTHIA DWT and HERWIG++ are shown in Figure 40. They agree within 5% (2%) at r=0.1 (0.2) for $60 < p_{\mathrm{T}} < 80$ GeV. For $p_{\mathrm{T}} > 80$ GeV the differences range between $5-10$% at r=0.1 and are less than 5% at r=0.2. These differences decrease with increasing radius r for all jet p_{T}.

The correction factors have been also compared for PYTHIA DWT and PYTHIA DW simulations. The differences are less than 20% at r=0.1 and $<$ 10% at $r = 0.2$. For differential jet shapes at large r, they can be as large as $20-30$%. For integrated jet shapes, they become smaller for the high p_{T} jets and decrease with increasing r. The comparisons of correction factors for PYTHIA DWT and PYTHIA DW are shown in Figure 41 for differential jet shapes and in Figure 42 for integrated jet shapes.

14.3 Non-linearity of Calorimeter Response and Transverse Shower Profile

The uncertainties due to CMS calorimeter simulation can be estimated by comparing track jet shapes with calorimeter jet shapes in simulated and collider data. Here we assume that track reconstruction inefficiency and fake rate are small in both data and MC and have negligible effect on track jet shapes. In addition, it is assumed that any difference in calorimeter response to photons in data and MC is much smaller than possible difference in calorimeter response to hadrons. The track jetshapes are compared to calorimeter jetshapes in Figure 43 for data and the PYTHIA predictions. These ratios, under above assumptions, show the effective calorimeter

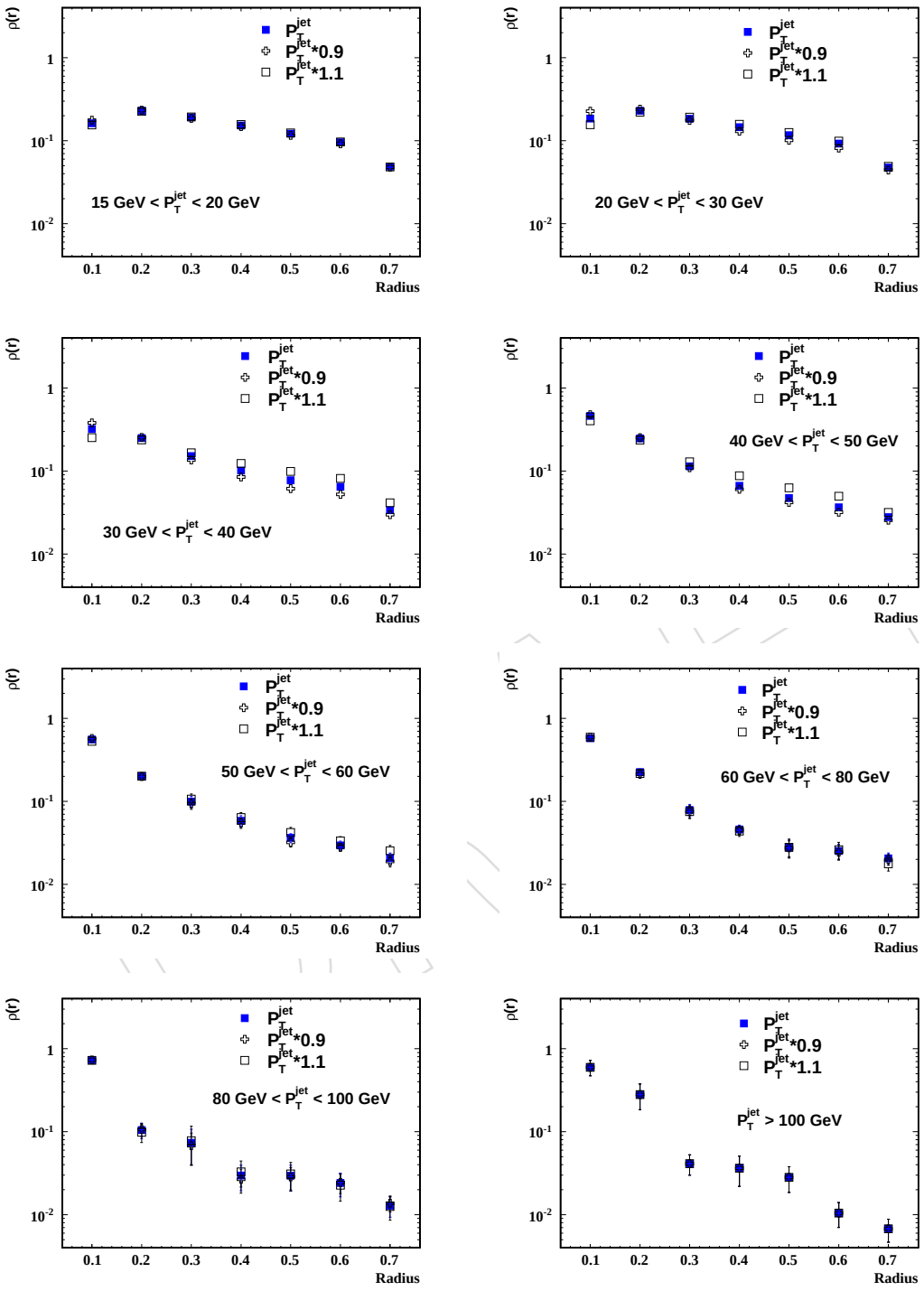

Figure 33: The fractional change in the differential jetshapes due to uncertainty in the jet energy scale determined by changing the jet energy scale by $\pm 10\%$ independent of jet p_{T} and y.

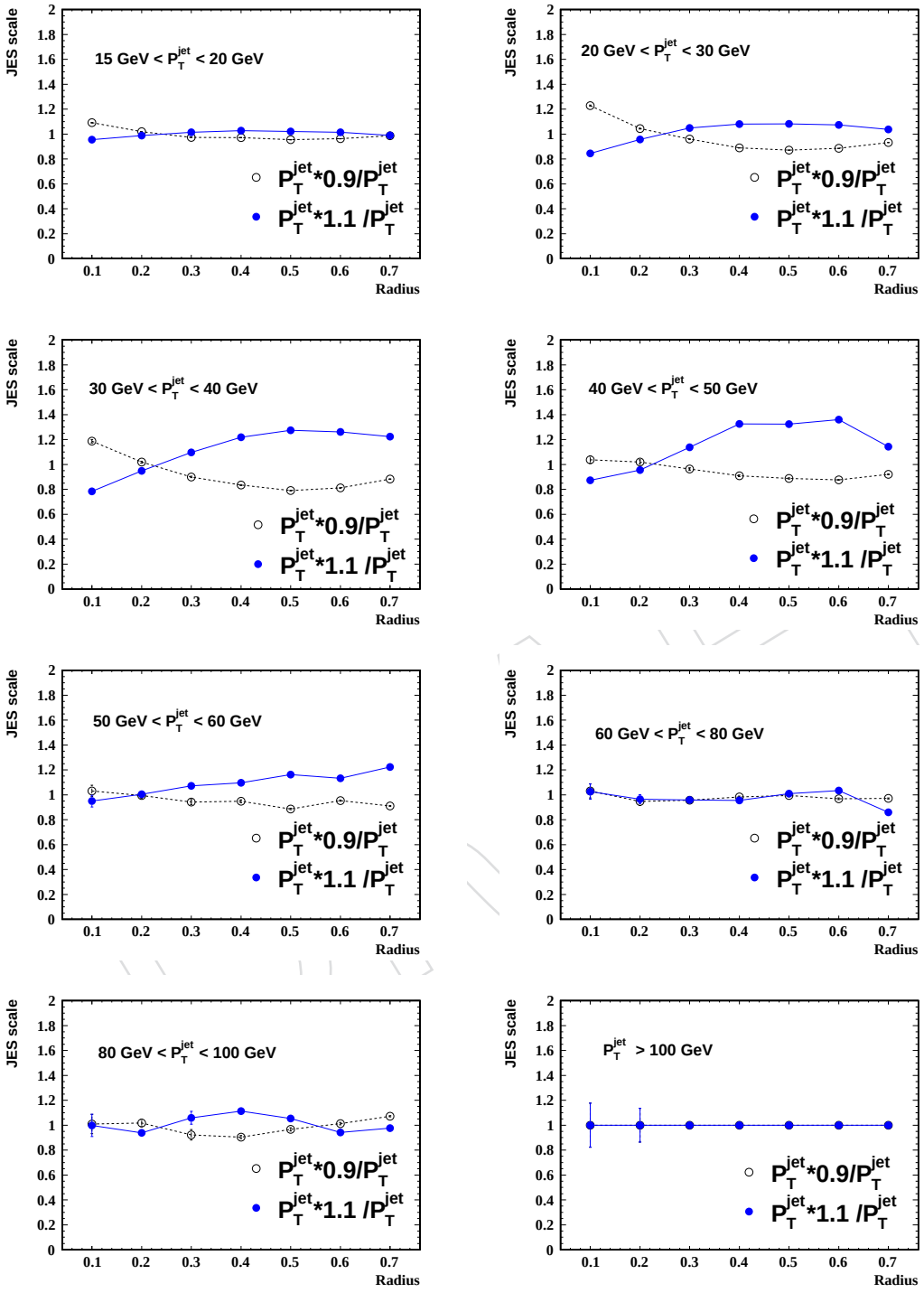

Figure 34: The fractional change in the differential jetshapes due to uncertainty in the jet energy scale determined by changing the jet energy scale by $\pm 10\%$ independent of jet p_{T} and y.

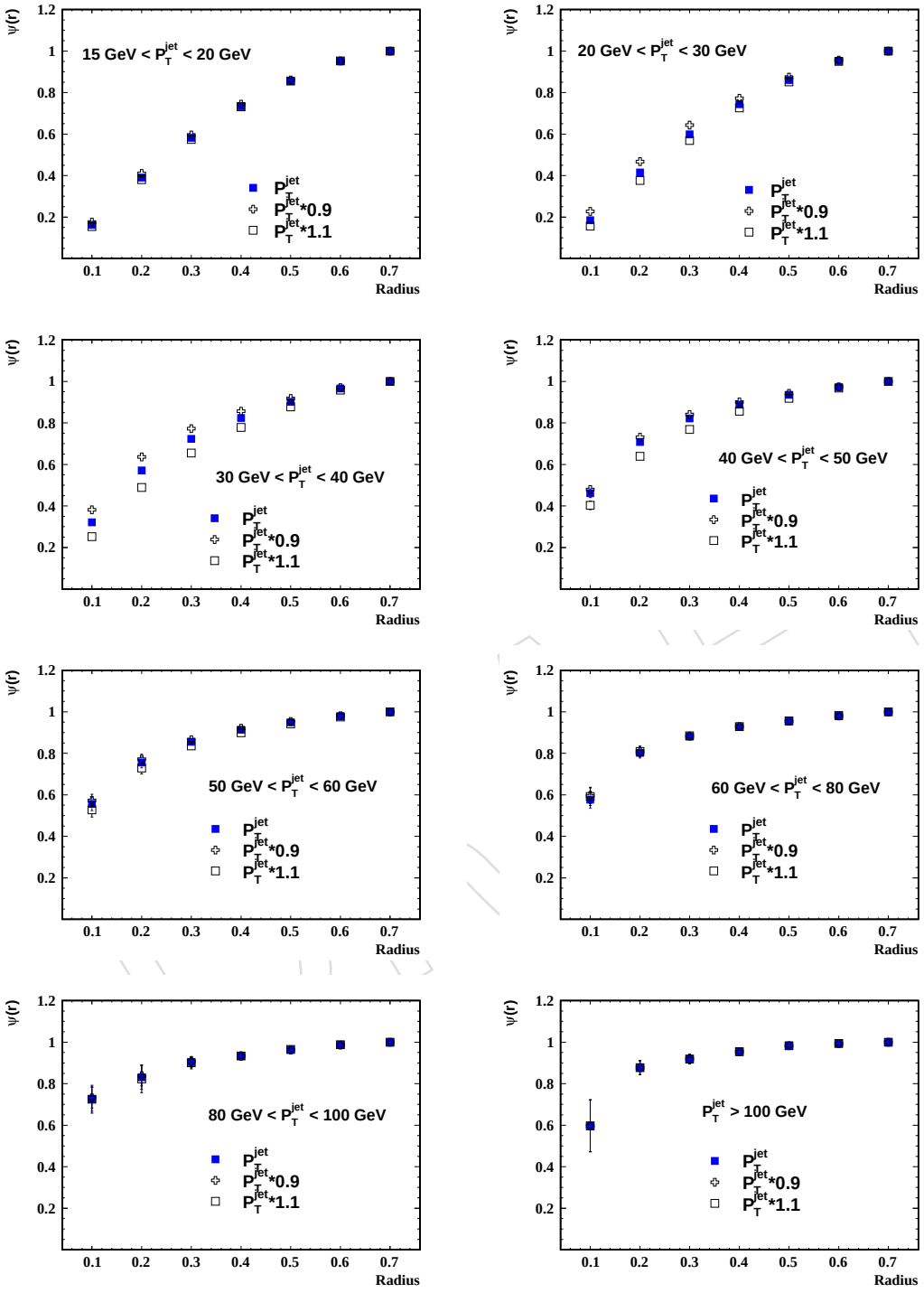

Figure 35: The fractional change in the integrated jetshapes due to uncertainty in the jet energy scale determined by changing the jet energy scale by $\pm 10\%$ independent of jet p_{T} and y.

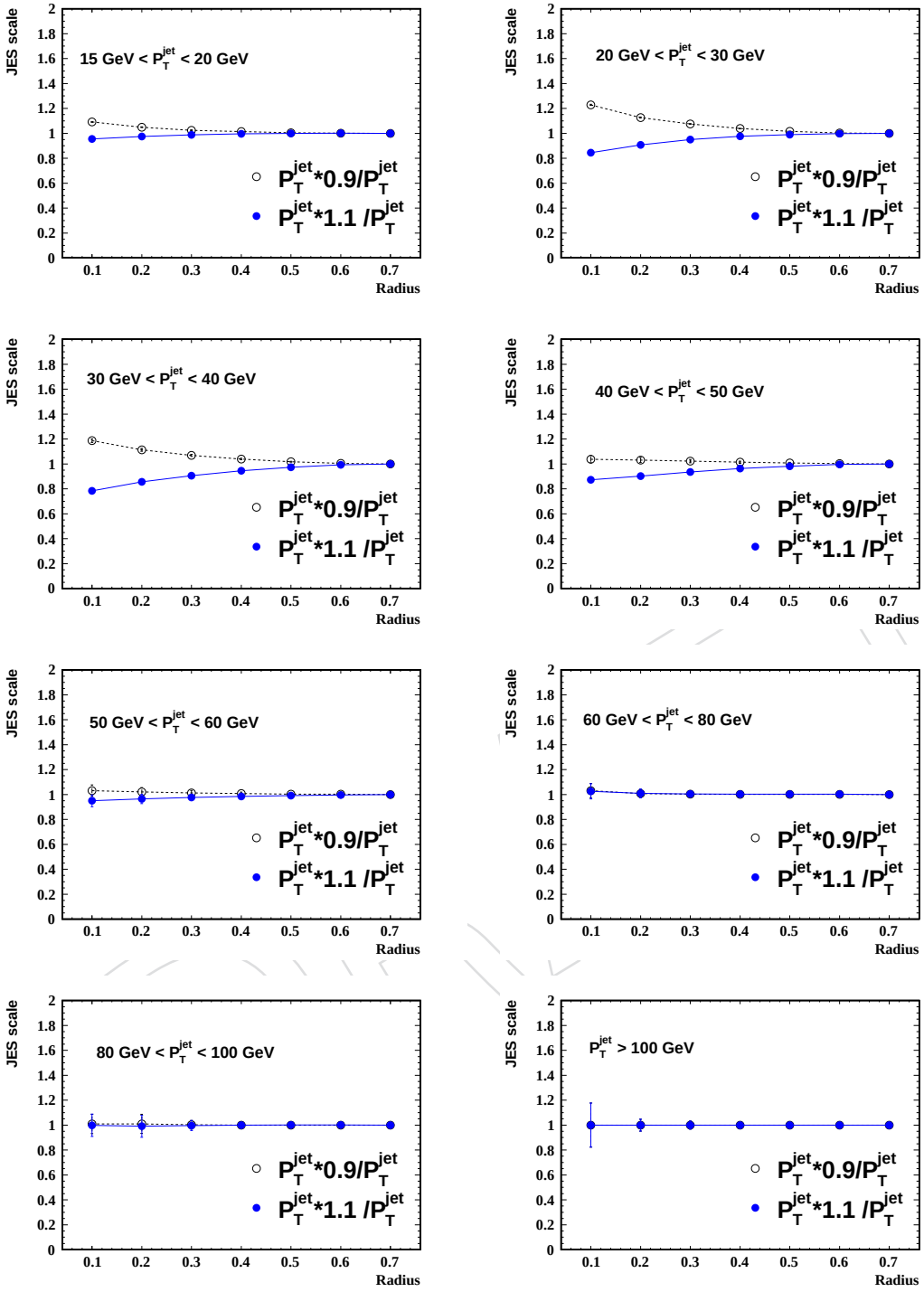

Figure 36: The fractional change in the integrated jetshapes due to uncertainty in the jet energy scale determined by changing the jet energy scale by $\pm 10\%$ independent of jet p_{T} and y.

Figure 37: Particle level differential jetshapes as predicted by PYTHIA and HERWIG event generators for selected $p_{\mathrm{T}}^{\mathrm{Jet}}$ bins.

Figure 38: Particle level integral jetshapes as predicted by PYTHIA and HERWIG event generators for selected $p_{\mathrm{T}}^{\mathrm{Jet}}$ bins.

Figure 39: Corrections factor for differential jetshapes as determined from PYTHIA and HERWIG event generators for selected $p_{\mathrm{T}}^{\mathrm{Jet}}$ bins.

response to particles as a function of r. The two responses are very close. The difference is assigned as the systematic uncertainty on the observed jetshapes.

As shown in Fig' **??**, the scale factor SF as defined below is very close to 1.0 showing that calorimeter simulation describes the observed calorimeter response very well.The difference from unity is assigned as systematic uncertainty. and the deviation from unity is assigned as the systematic uncertainty. At large r, the particles are very soft. Some of the particles do not reach the calorimeter. The calorimeter response to the particles which do reach the calorimeter is low. Thus the ratio of calo-jetshapes to track-jetshape is large. Analogous procedure is used for the integrated jet shapes (see Fig. 44.)

$$SF = \frac{R^{DATA}}{R^{MC}} \quad \text{where} \quad R^{MC} = \left.\frac{TrackJetShape}{CaloJetShape}\right|_{MC},\ R^{DATA} = \left.\frac{TrackJetShape}{CaloJetShape}\right|_{DATA} \tag{8}$$

15 Conclusions

We have measured differential and integrates jetshapes of the jets with $15 < p_{\mathrm{T}} < 150$ GeV in $|y| < 1.0$ region produced in pp collisions at $\sqrt{s} = 7$ TeV. These jets becomes narrow with increasing jet transverse momentum, in good agreement with QCD inspired event generators, PYTHIA and HERWIG. The observed jetshapes are closer to gluon jetshapes at low p_{T} and tend toward quark jetshapes at high p_{T}. A comparison of these jetshapes with different PYTHIA tunes shows that these data prefer **CW** tune.

Several sources of systematic uncertainties were investigated, arising from jet energy calibration, jet fragmentation, calorimeter response and transverse showering, as function of jet p_{T} and distance from jet axis r. The systematic uncertainty is dominated by overall jet energy scale, jet fragmentation and calorimeter simulation effects. The total systematic uncertainty at r=0.2 is 12% at p_{T} =60 GeV, decreasing to 4% at jet p_{T} =1 TeV.

Figure 40: Corrections factor for differential jetshapes as determined from PYTHIA and HERWIG event generators for selected $p_{\mathrm{T}}^{\mathrm{Jet}}$ bins.

Figure 41: Corrections factor for differential jetshapes determined using two different tunes of the PYTHIA event generator for selected $p_{\mathrm{T}}^{\mathrm{Jet}}$ bins.

Figure 42: Corrections factor for integral jetshapes determined using two different tunes of the PYTHIA event generator for selected $p_{\mathrm{T}}^{\mathrm{Jet}}$ bins.

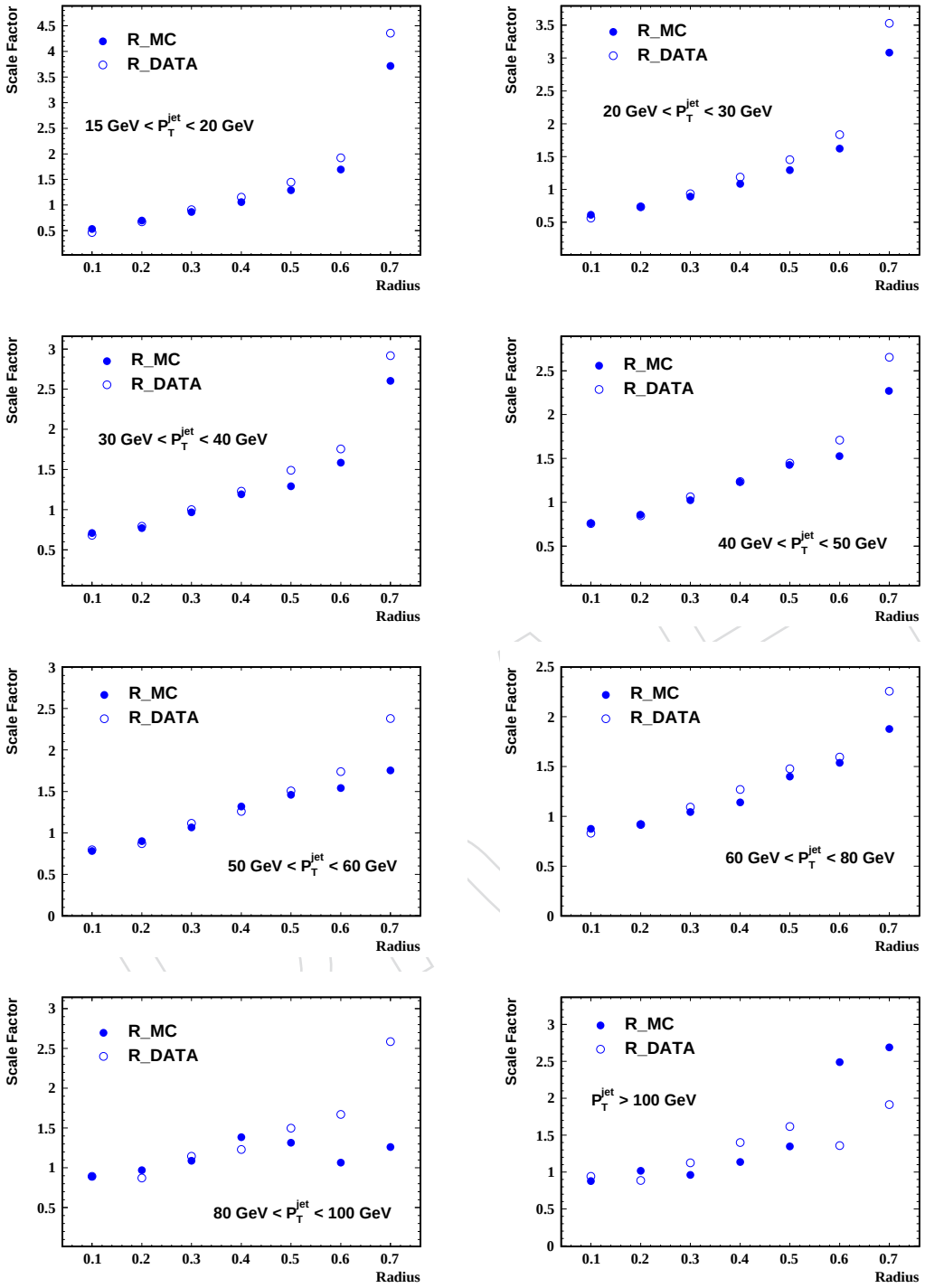

Figure 43: The ratio of calorimeter differential jetshapes to track differential jetshapes measured after propogating the tracks to calorimeter surface for data and Pythia MC.

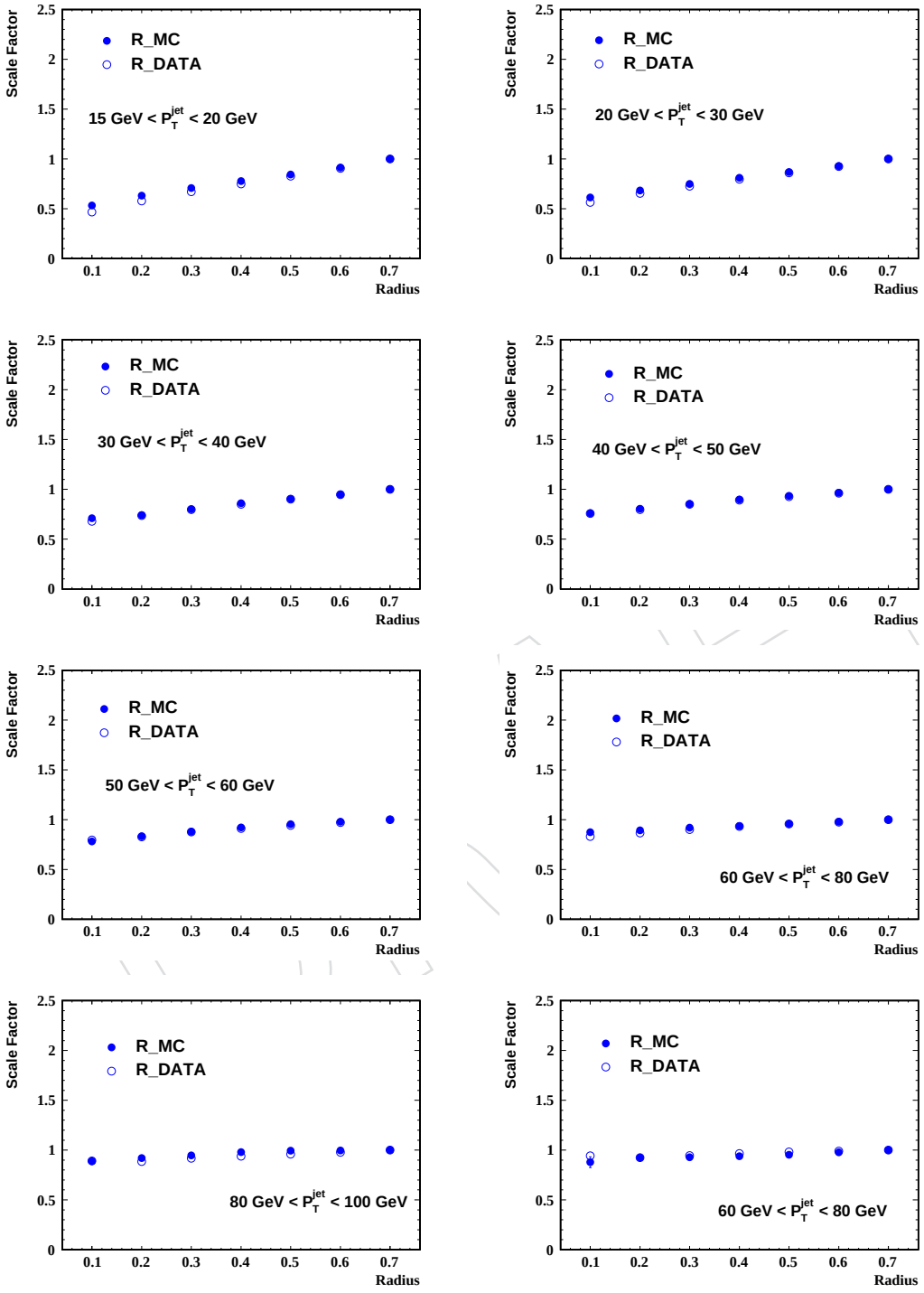

Figure 44: The ratio of calorimeter integrated jetshapes to track integrated jetshapes measured after propogating the tracks to calorimeter surface for data and Pythia MC.

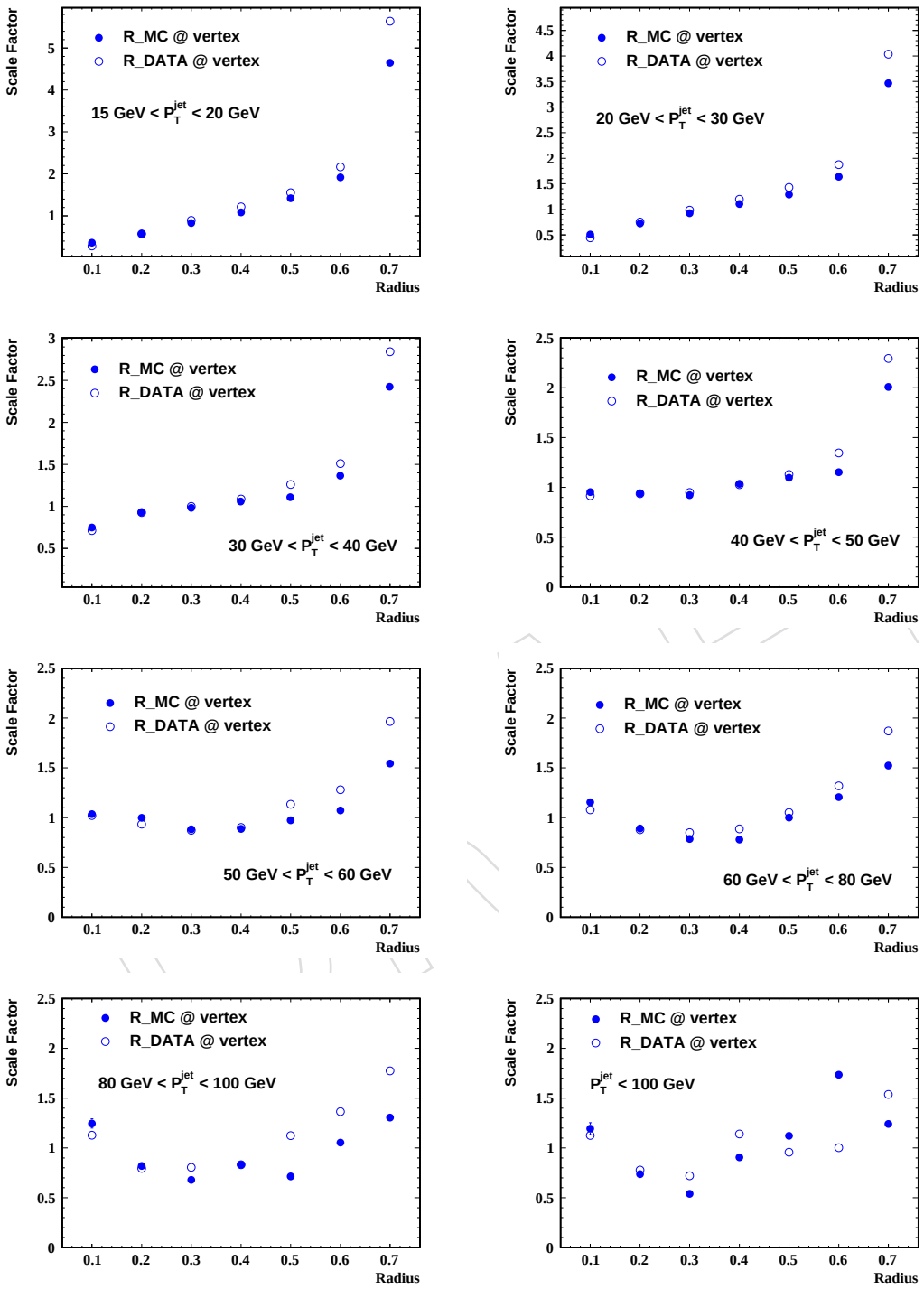

Figure 45: The ratio of calorimeter differential jetshapes to track differential jetshapes measured after propogating the tracks to calorimeter surface for data and Pythia MC.

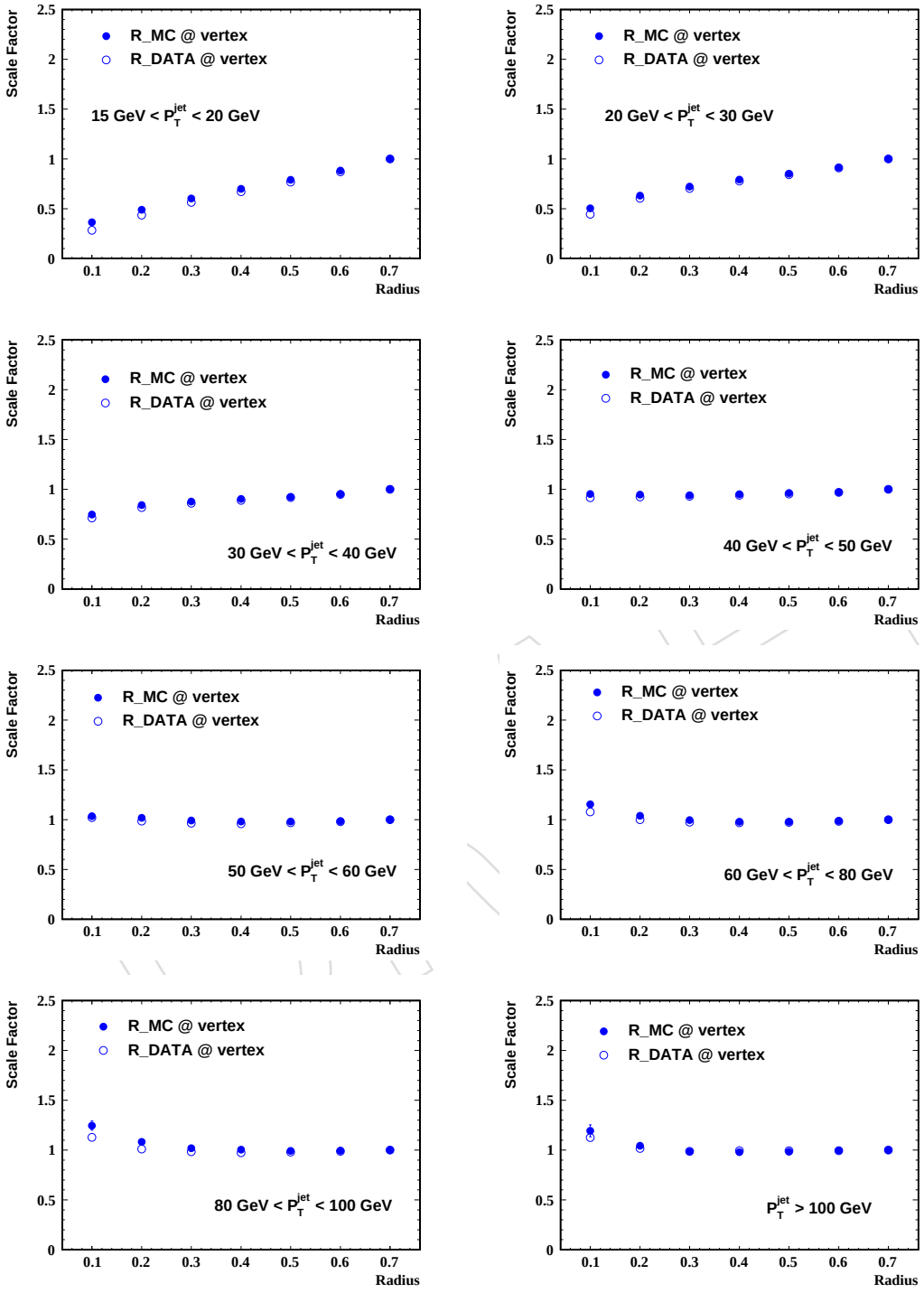

Figure 46: The ratio of calorimeter integrated jetshapes to track integrated jetshapes measured after propogating the tracks to calorimeter surface for data and Pythia MC.

GeV	N^{Jets}	N_p	$< \psi(r = 0.2) >$	rms	$\sigma = rms/\sqrt{N_p}$	$\sigma / < \psi(r = 0.2) > (\%)$
15-20	5313					
20-30	4333					
30-40	1147					
40-50	403					
50-60	210					
60-80	101					
80-100	41					
100-	16					

Table 1: Number of jets before and after prescale, and mean and rms values of the p_T fraction histograms at r=0.2 in 10 pb^{-1} for all p_{T} jet bins which were analyzed. Statistical errors are listed for the corresponding jet p_{T} using prescaled event numbers.

Table 2: Different sources of systematics for $\psi(r = 0.2)$ listed as percentage contributions for all jet p_{T} bins for 10 pb^{-1} of integrated luminosity. Total systematics is a quadrature sum of fragmentation, jet energy scale, showering and E/p contributions.

p_{T} (GeV)	$Fragmentation(\%)$	$JES(\%)$	$Showering(\%)$	$E/p(\%)$	$TotalSys.(\%)$

Table 3: Absolute error on $1 - \psi(r = 0.2)$ represents quadratic sum of systematic and statistical uncertainties for 10 pb^{-1} of integrated luminosity. $I(r = 0.2)$ refers to the integrated correction factors at r=0.2.

p_{T} GeV	Raw $\psi(r = 0.2)$	$I(r = 0.2)$	$1 - \psi(r = 0.2)$	$AbsErr$
$15 - 20$	0.66	0.90	0.41	0.072

References

[1] S. D. Ellis, Z. Kunszt, and D. E. Soper, "Jets at hadron colliders at order alpha-s**3: A Look inside", *Phys. Rev. Lett.* **69** (1992) 3615–3618, arXiv:hep-ph/9208249. doi:10.1103/PhysRevLett.69.3615.

[2] M. H. Seymour, "Jet shapes in hadron collisions: Higher orders, resummation and hadronization", *Nucl. Phys.* **B513** (1998) 269–300, arXiv:hep-ph/9707338. doi:10.1016/S0550-3213(97)00711-6.

[3] CDF Collaboration, "A Measurement of jet shapes in $p\bar{p}$ collisions at $\sqrt{s} = 1.8$ TeV", *Phys. Rev. Lett.* **70** (1993) 713–717. doi:10.1103/PhysRevLett.70.713.

[4] D0 Collaboration, "Transverse energy distributions within jets in $p\bar{p}$ collisions at $\sqrt{s} = 1.8$ TeV", *Phys. Lett.* **B357** (1995) 500–508. doi:10.1016/0370-2693(95)00889-S.

[5] CDF Collaboration, "Study of jet shapes in inclusive jet production in $p\bar{p}$ collisions at $\sqrt{s} = 1.96$ TeV", *Phys. Rev.* **D71** (2005) 112002, arXiv:hep-ex/0505013. doi:10.1103/PhysRevD.71.112002.

[6] H1 Collaboration, "Measurements of transverse energy flow in deep inelastic scattering at HERA", *Eur. Phys. J.* **C12** (2000) 595–607, arXiv:hep-ex/9907027. doi:10.1007/s100520000287.

[7] ZEUS Collaboration, "Measurement of jet shapes in high-Q**2 deep inelastic scattering at HERA", *Eur. Phys. J.* **C8** (1999) 367–380, arXiv:hep-ex/9804001. doi:10.1007/s100520050471.

[8] CMS Collaboration, " The Compact MUon Solenoid (CMS) Technical Proposal",. CERN/LHCC 94-38.

[9] CMS Collaboration, "CMS TDR4",. CERN/LHCC 97-33.

[10] CMS Collaboration, "CMS TDR2",. CERN/LHCC 97-31.

[11] The coordinate system used at CMS is defined as follows: the x-axis points horizontally outside the LHC ring, the y-axis points upwards, and the z-axis is aligned with the nominal beam direction. The azimuthal angle is ϕ and the polar angle is θ. The transverse momentum P_T is defined as a projection of a particle momentum P on the xy-plane, $P_T = P \cdot \sin\theta$. The rapidity is defined as $y = \frac{1}{2} \log \frac{E+P_Z}{E-P_Z}$, where E denotes the energy and P_Z is the component of the momentum along the z direction.

[12] G. P. Salam, "A Practical Seedless Infrared Safe Cone Algorithm", arXiv:0705.2696.

[13] M. Cacciari, G. P. Salam, and G. Soyez, "The anti-k_T jet clustering algorithm", *JHEP* **04** (2008) 063, arXiv:0802.1189. doi:10.1088/1126-6708/2008/04/063.

[14] CMS Collaboration, "Comparison of Single Particle Response in Data and MC at 900 GeV",. CMS AN-2010/072.

[15] CMS Collaboration, "The Underlying Event at LHC",. CMS-Note-2006/067.

[16] CMS Collaboration, "Plans for Jet Energy Corrections at CMS",. CMS-PAS-JME-007-002.

[17] M. Bahr, S. Gieseke, and M. H. Seymour, "Simulation of multiple partonic interactions in Herwig++", *JHEP* **07** (2008) 076, arXiv:0803.3633. doi:10.1088/1126-6708/2008/07/076.

[18] M. Bahr et al., "Herwig++ 2.2 Release Note", arXiv:0804.3053.